*J. Fluid Mech.* (2012), *vol.* 694, *pp.* 292–331.  
doi:10.1017/jfm.2011.548

# Dynamics of vorticity defects in stratified shear flow

**N. J. Balmforth[1,2], A. Roy[3] and C. P. Caulfield[4,5]†**

[1] Department of Mathematics, University of British Columbia, 1984 Mathematics Road, Vancouver, BC, V6T 1Z2, Canada

[2] Department of Earth and Ocean Science, University of British Columbia, 6339 Stores Road, Vancouver, BC, V6T 1Z4, Canada

[3] Engineering Mechanics Unit, Jawaharlal Nehru Centre for Advanced Scientific Research, Bangalore, India

[4] BP Institute for Multiphase Flow, University of Cambridge, Madingley Rise, Madingley Road, Cambridge CB3 0EZ, UK

[5] Department of Applied Mathematics & Theoretical Physics, University of Cambridge, Centre for Mathematical Sciences, Wilberforce Road, Cambridge CB3 0WA, UK

(Received 7 September 2011; revised 5 December 2011; accepted 12 December 2011; first published online 25 January 2012)

We consider the linear stability and nonlinear evolution of two-dimensional shear flows that take the form of an unstratified plane Couette flow that is seeded with a localized 'defect' containing sharp density and vorticity variations. For such flows, matched asymptotic expansions furnish a reduced model that allows a straightforward and computationally efficient exploration of flows at sufficiently high Reynolds and Péclet numbers that sharp density and vorticity gradients persist throughout the onset, growth and saturation of instability. We are thereby able to study the linear and nonlinear dynamics of three canonical variants of stratified shear instability: Kelvin–Helmholtz instability, the Holmboe instability, and the lesser-considered Taylor instability, all of which are often interpreted in terms of the interactions of waves riding on sharp interfaces of density and vorticity. The dynamics near onset is catalogued; if the interfaces are sufficiently sharp, the onset of instability is subcritical, with a nonlinear state existing below the linear instability threshold. Beyond onset, both Holmboe and Taylor instabilities are susceptible to inherently two-dimensional secondary instabilities that lead to wave mergers and wavelength coarsening. Additional two-dimensional secondary instabilities are also found to appear for higher Prandtl numbers that take the form of parasitic Holmboe-like waves.

**Key words:** instability, shear layers, stratified flows

## 1. Introduction

Stratified shear flow instability plays a key role in a wide range of geophysical phenomena, in particular as a route to turbulence and hence enhanced mixing (see for example the recent review of Ivey, Winters & Koseff 2008). The most commonly observed and explored variant is the Kelvin–Helmholtz (KH) instability, popularly

† Email address for correspondence: c.p.caulfield@bpi.cam.ac.uk

known for its overturning billowing patterns and its ability to mix effectively (although not necessarily particularly efficiently; cf. Peltier & Caulfield 2003). However, stratified shear flows are also susceptible to a number of other, much less-commonly considered instabilities.

The mechanism behind the KH instability is sometimes described in terms of the interaction of waves riding on localized, strong gradients, or interfaces, of vorticity. With the inclusion of additional interfaces of sharp density variation, two other prominent shear flow instabilities can be classified (Baines & Mitsudera 1994; Caulfield 1994; Carpenter, Balmforth & Lawrence 2010*a*): the Holmboe instability, arising due to the interaction between a 'vorticity' wave and a wave riding on a density interface (Holmboe 1962; Alexakis 2005); and the 'Taylor' instability (considered in Taylor 1931) due to interaction between interfacial density waves and coupled by the ambient shear flow. Of these second two instabilities, only the Holmboe case has received detailed attention, with numerical simulations (e.g. Smyth, Klaassen & Peltier 1988; Smyth & Winters 2003; Carpenter *et al.* 2010*b*) and laboratory experiments (e.g. Thorpe 1971; Yoshida *et al.* 1998; Zhu & Lawrence 2001; Hogg & Ivey 2003; Tedford, Pieters & Lawrence 2009) elucidating some of its character. By contrast, aside from Taylor's 1931 original paper, a much later analysis outlining its linear stability properties (Caulfield 1994), a speculative experimental observation (Caulfield *et al.* 1995) and a brief numerical exploration (Lee & Caulfield 2001), the Taylor instability remains unexplored.

Although it is neither necessary nor, at times, useful to characterize stratified shear instability in terms of different kinds of interfacial wave interactions, the notion proves convenient in view of the common occurrence of 'staircases' in geophysical flows: stacked sequences of unstratified layers separated by sharp interfaces of high density gradient (e.g. Linden 1979; Schmitt 1994). With this in mind, the current study is aimed at providing a compact exploration of the three kinds of instabilities listed above. For this task, rather than attacking the full, governing equations of stratified fluid dynamics, a long-winded numerical exercise at best, we exploit some convenient idealizations and simplifications.

First, we restrict attention to two spatial dimensions which, in view of the known dynamics of three-dimensional KH instability (Caulfield & Peltier 2000; Smyth & Moum 2000; Staquet 2000), likely limits the applicability of our solutions to the initial stages of the development of all three instabilities, and precludes us from studying any kind of turbulent transition. Second, we focus on specific kinds of stratified shear flows for which asymptotic methods can be used to reduce the governing equations to a more manageable form. These stratified vorticity 'defects', motivated originally by Gill (1965), are illustrated in figure 1; the flows consist of an unstratified, uniform shear flow that is seeded with an embedded, localized region (the defect) containing finely scaled vorticity and density variations. The defect structure allows one to exploit matched asymptotic expansions to furnish a reduced model of the dynamics, and has been successfully applied to studies of unstratified shear flows (Balmforth, del Castillo-Negrete & Young 1997; Balmforth 1998). The key simplifications afforded by the 'defect approximation' are a compact and tractable version of linear theory and a swifter construction of analytical and numerical nonlinear solutions.

The current, stratified defect analysis leads us to our relatively concise exploration of the dynamics of two-dimensional KH, Holmboe and Taylor instabilities. We summarize the key features of these 'primary' instabilities, surveying, in particular, how the instabilities first appear, and document a variety of secondary instabilities that they suffer. Although our calculations are restricted to two dimensions, we believe

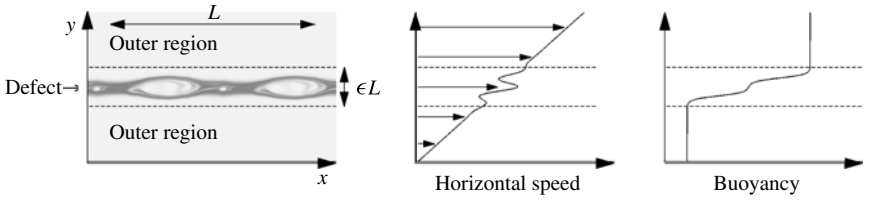


FIGURE 1. A stratified defect. The first picture shows the overall geometry, with an illustration of the expected vortical structure (actually a solution of the defect equations). The other graphs illustrate the horizontal velocity and buoyancy of equilibrium defects.

it is still valuable to document these secondary instabilities, as numerical evidence (see for example Mashayek & Peltier 2011*b*) demonstrates that inherently two-dimensional secondary instabilities (such as subharmonic merging, or the secondary shear instability predicted by Corcos & Sherman 1976 to occur in the 'braid' between neighbouring primary KH billow cores) develop and 'compete' with inherently three-dimensional secondary instabilities in stratified shear layers. Our discussion is organized as follows: in § 2, we develop the stratified defect formulation. Section 3 presents linear stability calculations for inviscid, non-diffusive defects, demonstrating that the model captures salient details of all three primary instabilities. In § 4, we investigate numerically the initial-value problem for flows prone to each of the three primary instabilities. Section 5 draws some brief conclusions.

## 2. Defect formulation

We begin with the vorticity–buoyancy–streamfunction formulation for two-dimensional stratified fluid in the Boussinesq approximation: we denote the streamfunction, vorticity and buoyancy by $\hat{\psi}(\hat{x},\hat{y},\hat{t})$, $\hat{\zeta}(\hat{x},\hat{y},\hat{t})$ and $\hat{b}(\hat{x},\hat{y},\hat{t})$, respectively, where $\hat{t}$ is time, and the fluid is described by a Cartesian coordinate system, $(\hat{x},\hat{y})$, in which $\hat{y}$ points vertically upwards. The governing equations are

$$\hat{\zeta} = \hat{\psi}_{\hat{x}\hat{x}} + \hat{\psi}_{\hat{y}\hat{y}}, \tag{2.1}$$

$$\zeta_{\hat{t}} + \hat{\psi}_{\hat{x}}\hat{\zeta}_{\hat{y}} - \hat{\psi}_{\hat{y}}\hat{\zeta}_{\hat{x}} = \hat{b}_{\hat{x}} + \hat{\nu}(\hat{\zeta}_{\hat{x}\hat{x}} + \hat{\zeta}_{\hat{y}\hat{y}}), \tag{2.2}$$

$$\hat{b}_{\hat{t}} + \hat{\psi}_{\hat{x}}\hat{b}_{\hat{y}} - \hat{\psi}_{\hat{y}}\hat{b}_{\hat{x}} = \hat{\kappa}(\hat{b}_{\hat{x}\hat{x}} + \hat{b}_{\hat{y}\hat{y}}), \tag{2.3}$$

where $\hat{\nu}$ is the kinematic viscosity and $\hat{\kappa}$ the diffusivity. The velocity field is given by $(u,v) = (-\hat{\psi}_{\hat{y}}, \hat{\psi}_{\hat{x}})$, and the density perturbations are $\rho_0\hat{b}/g$, with $g$ being gravity and $\rho_0$ a reference density.

To render the system dimensionless, we introduce a characteristic length scale, $L$, and speed, $U$, chosen as follows: we consider an infinitely deep fluid with an ambient shear flow that is largely linear in height: $u \approx s\hat{y}$, where $s$ is a prescribed shear rate. Hence, we may define $U = sL$, given $L$. In earlier studies (Balmforth *et al.* 1997; Balmforth 1998), the problem was couched in a channel of finite width, introducing one choice for $L$. Here, however, we consider an infinitely deep flow (or at least a very tall channel for which the channel height is irrelevant), seeded with a vertically localized defect (figure 1) that we centre at the origin of our coordinate system ($\hat{y} = 0$). We further consider spatially periodic flows in the horizontal, which allows us to use the domain length as a more natural characteristic scale. In particular, by setting the domain length equal $2\pi L$, we couch the instability problem in a dimensionless domain of length $2\pi$. The defect, on the other hand, is much shallower, and we define $\epsilon \ll 1$

to be the ratio of the vertical thickness of the defect and $L$ (see figure 1). In this sense, our theory is a long-wave one, and $\epsilon$ is the small parameter we use to organize an asymptotic analysis.

Given these characteristic scales, we define the dimensionless variables,

$$(x, y) = L^{-1}(\hat{x}, \hat{y}), \quad t = L^{-1}U\epsilon\hat{t}, \tag{2.4}$$

$$\hat{\psi} = -\frac{1}{2}ULy^2 + \epsilon^2 UL\psi(x, y, t), \quad \hat{\zeta} = \frac{U}{L} + \epsilon^2\frac{U}{L}\zeta(x, y, t), \quad \hat{b} = \epsilon^2\frac{U^2}{L}b(x, y, t). \tag{2.5}$$

By scaling time, streamfunction, vorticity and buoyancy in this way, we prepare the equations for the asymptotic expansion given in the next section; from the physical perspective, the scaling focuses attention on the relatively long and weakly nonlinear evolution of the defect, filtering any dynamics from outside that region. The dimensionless versions of (2.1)–(2.3) are then

$$\psi_{xx} + \psi_{yy} = \zeta, \tag{2.6}$$

$$y\zeta_x + \epsilon\zeta_t + \epsilon^2\psi_x\zeta_y - \epsilon^2\psi_y\zeta_x - \epsilon^3\nu(\zeta_{xx} + \zeta_{yy}) = b_x, \tag{2.7}$$

$$yb_x + \epsilon b_t + \epsilon^2\psi_x b_y - \epsilon^2\psi_y b_x - \epsilon^3\kappa(b_{xx} + b_{yy}) = 0, \tag{2.8}$$

and the scaled, inverse Reynolds and Péclet numbers are

$$\nu = \frac{\hat{\nu}}{\epsilon^3 UL}, \quad \kappa = \frac{\hat{\kappa}}{\epsilon^3 UL}, \tag{2.9}$$

which are tuned so that the leading-order effect of viscosity and diffusion appears in the defect theory simultaneously with unsteadyness and nonlinearity.

The leading-order terms on the left of (2.7)–(2.8) account for advection by the background linear shear; as demonstrated shortly, the shorter vertical scale of the defect promotes some of the other terms to balance this advection over that region. Notably, although the vorticity is order $\epsilon^2$ outside the defect, it increases to $O(\epsilon)$ within the defect, and its vertical gradient is order unity there. These features mirror the original defect theory. The extension we make here is to add stratification, taking the density to be largely uniform outside the defect, but rapidly varying within it. Thus, from outside, the defect appears very much like a vortex sheet and a density interface.

### 2.1. *Matched asymptotics*

Equations (2.7)–(2.8) can be attacked using the method of matched asymptotic expansions. There is an outer region, outside the defect, where $y$ is order one. The inner region, the defect, must be resolved by introducing a new, inner coordinate, $\eta = y/\epsilon$. With the current defect structure, the matched asymptotics are a straightforward generalization of those used by Balmforth *et al.* (1997), and, for the most part, we require only the leading-order terms of the equations in each of the regions.

#### 2.1.1. *Outer solution; $y = O(1)$*

For the leading-order outer problem, we discard higher-order terms in (2.6)–(2.8), to arrive at

$$y\,(\psi_{xx} + \psi_{yy})_x \sim b_x \quad \text{and} \quad yb_x \sim 0. \tag{2.10}$$

We therefore take $b_x \sim O(\epsilon)$ outside the defect and solve the resulting Laplace equation for the streamfunction using a Fourier series:

$$\psi = \sum_{n=-\infty}^{\infty} \Phi_n(t) \mathrm{e}^{\mathrm{i}nx-|n|y} + \bar{\psi}(y,t), \tag{2.11}$$

where the horizontal average, $\bar{\psi}(y,t) = \int_0^{2\pi} \psi(x,y,t)\,\mathrm{d}x/(2\pi)$, and

$$\Phi(x,t) = \sum_{-\infty}^{\infty} \Phi_n(t) \mathrm{e}^{\mathrm{i}nx} \tag{2.12}$$

is a limiting streamfunction amplitude at the defect. This solution contains a jump in vertical derivative of

$$[\psi_y]_{y=0-}^{y=0^+} = -2 \sum_{n=-\infty}^{\infty} |n| \Phi_n \mathrm{e}^{\mathrm{i}nx} + [\bar{\psi}_y]_{y=0-}^{y=0^+}, \tag{2.13}$$

which accommodates the spatially confined vorticity inside the defect.

2.1.2. *Inner equations,* $\eta = y/\epsilon = O(1)$

Within the defect, $\eta = y/\epsilon$ is of order one, and we introduce the rescalings,

$$\psi = \varphi(x,\eta,t) = \varphi_0(x,t) + \epsilon\varphi_1(x,\eta,t), \quad \zeta = \epsilon^{-1} Z(x,\eta,t), \quad b = B(x,\eta,t). \tag{2.14}$$

The inner form of the vorticity–streamfunction relation is then

$$Z = \epsilon^{-1}\varphi_{\eta\eta} + \epsilon\varphi_{xx} \sim \varphi_{1\eta\eta}. \tag{2.15}$$

The promotion of the vertical derivatives in this relation is key in dictating that the streamfunction be independent of $\eta$ to leading order; the match with the outer solution then determines that leading order term (i.e. $\varphi_0(x,t) = \Phi(x,t) + \bar{\psi}(0,t)$). The jump in the vertical derivative of the outer solution, given by (2.13), must also be matched to the corresponding jump of the inner solution across the defect: from (2.15) it follows that

$$[\varphi_{1\eta}]_{\eta\to-\infty}^{\eta\to\infty} \equiv \int_{-\infty}^{\infty} Z(x,\eta,t)\,\mathrm{d}\eta. \tag{2.16}$$

Hence, after subtracting off the horizontal average,

$$\int_{-\infty}^{\infty} Z(x,\eta,t)\,\mathrm{d}\eta - \langle Z\rangle = -2\sum_{-\infty}^{\infty} |n| \Phi_n \mathrm{e}^{\mathrm{i}nx} =: \mathscr{L}\Phi, \tag{2.17}$$

where

$$\langle\cdots\rangle = \frac{1}{2\pi}\int_{-\infty}^{\infty}\int_0^{2\pi} (\cdots)\,\mathrm{d}x\,\mathrm{d}\eta. \tag{2.18}$$

Finally, we introduce (2.14) into (2.7)–(2.8), then retain only the leading-order terms, to arrive the defect vorticity and buoyancy equations,

$$Z_t + \eta Z_x + \Phi_x Z_\eta - \nu Z_{\eta\eta} = B_x, \tag{2.19}$$

$$B_t + \eta B_x + \Phi_x B_\eta - \kappa B_{\eta\eta} = 0. \tag{2.20}$$

Equations (2.17)–(2.20) constitute the reduced equations for stratified vorticity defects. In addition to periodicity in $x$, the requirement to match with the outer

solution furnishes the boundary conditions,

$$Z_x \to 0, \quad B_x \to 0 \quad \text{as } \eta \to \pm\infty. \tag{2.21}$$

The system offers a concise description of linear stability of the defect, and allows us to explore its nonlinear dynamics with numerical computations. Note that the small parameter no longer appears in the defect formulation, and the key field variables, $Z(x, \eta, t)$ and $B(x, \eta, t)$, are defined in terms of the stretched vertical coordinate $\eta = y/\epsilon$. Only when the original vorticity and buoyancy fields are reconstructed does $\epsilon$ reappear, and provided that parameter is taken sufficiently small for the reconstruction, the defect approximation remains valid. The most serious challenge to maintaining the fidelity of the approximation during the reconstruction is when the dynamics generates overly fine horizontal scales in the defect solutions (requiring $\epsilon$ to be made smaller to preserve the shallow aspect ratio).

### 2.2. *The $\nu = \kappa$ system*

The system in (2.17)–(2.20) cannot be reduced any further if $\kappa \neq \nu$, leaving us with three equations for the defect variables, $\Phi$, $Z$ and $B$ (i.e. the appropriately scaled streamfunction, vorticity and buoyancy, respectively). However, if the Prandtl number, $\nu/\kappa$, equals unity, then the variable,

$$\mathscr{Z}(x, \eta, t) \equiv Z(x, \eta, t) + B_\eta(x, \eta, t), \tag{2.22}$$

satisfies the reduced system,

$$\mathscr{Z}_t + \eta \mathscr{Z}_x + \Phi_x \mathscr{Z}_\eta - \nu \mathscr{Z}_{\eta\eta} = 0, \quad \mathscr{L}\Phi = \int_{-\infty}^{\infty} \mathscr{Z}(x, \eta, t)\, \mathrm{d}\eta - \langle \mathscr{Z} \rangle, \tag{2.23}$$

which is identical to the model for unstratified defects and is closely related to the Vlasov–Poisson system of plasma physics (e.g. Nicholson 1983; Balmforth *et al.* 1997).

Although the reduction to (2.23) suggests a major simplification of the system, it is not as useful as it might at first seem: one must still solve (2.19)–(2.20) in order to reconstruct the vorticity and buoyancy fields. The precise physical meaning of the combination in $\mathscr{Z}$ is somewhat opaque, but this quantity is evidently able to capture the main interplay between the outer shear and the fine structure of the vorticity and buoyancy distribution in the defect. As we shall see in the next section, ideal (inviscid and non-diffusive) instability hinges solely on the equilibrium distribution of $\mathscr{Z}$. Thus, all three types of instability (KH, Holmboe and Taylor) in the defect model are merely different forms of the instability of the $\mathscr{Z}$ distribution.

### 2.3. *Conservation laws and nonlinear waves*

Both (2.19) and (2.20) take the form of advection equations in the inviscid and non-diffusive limit, $(\nu, \kappa) \to 0$, with a total streamfunction given by

$$\Psi = \Phi - \tfrac{1}{2}\eta^2. \tag{2.24}$$

There are a number of conservation laws:

$$\frac{\mathrm{d}}{\mathrm{d}t}\langle Z \rangle = 0, \quad \frac{\mathrm{d}}{\mathrm{d}t}\langle \eta Z \rangle = 0, \tag{2.25}$$

and

$$\frac{\mathrm{d}}{\mathrm{d}t}\left\langle \frac{1}{2}(\eta^2 - \Phi)Z - \eta B \right\rangle = \nu \langle Z \rangle, \tag{2.26}$$

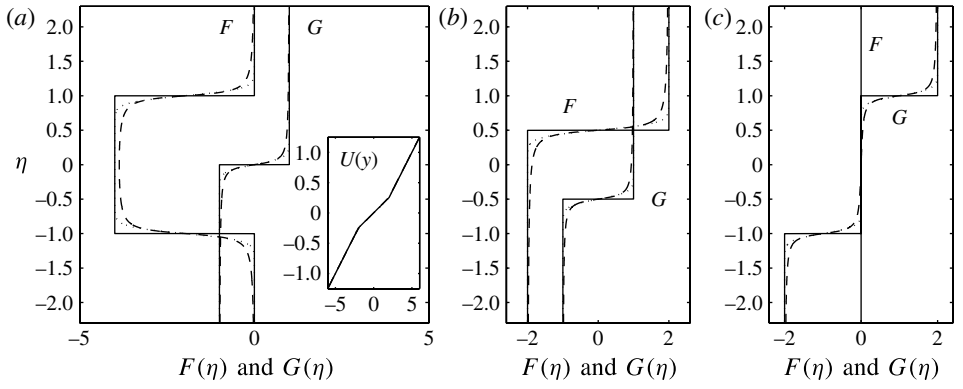


FIGURE 2. Sample defect equilibria for (*a*) profiles (3.4), (*b*) profiles (3.12) and (*c*) profiles (3.14), all with $f = 4$ and $\gamma = 2$. In each case, the solid line shows the broken-line version of the profile using (3.5), the dashed line shows the Lorentzian case with (3.6) and $\delta = 0.05$, and the dotted line is (3.7) with $\delta = 0.1$. The inset in (*a*) sketches the overall velocity profiles, $U(y)$, suggested by the vorticity defects in the main panel with $\epsilon = 1/4$.

which correspond to conservation of vorticity, horizontal momentum and energy (at least when $\nu = 0$). In addition to conservation of mass, $\langle B\rangle_t = 0$, when there is no viscosity or diffusion of density ($\nu = \kappa = 0$), there are an infinite number of invariant functionals:

$$\frac{\mathrm{d}}{\mathrm{d}t}\langle Z\mathscr{C}(B)\rangle = 0, \quad \frac{\mathrm{d}}{\mathrm{d}t}\langle \mathscr{D}(B)\rangle = 0, \tag{2.27}$$

where $\mathscr{C}(B)$ and $\mathscr{D}(B)$ are arbitrary functions of the defect density.

In the same limit, the steady travelling-wave equilibria are given by

$$\Psi_c = \Phi(x - ct) - \tfrac{1}{2}(\eta - c)^2, \quad B = \mathscr{B}(\Psi_c), \quad Z = \mathscr{Z}(\Psi_c) - (\eta - c)\mathscr{B}'(\Psi_c), \tag{2.28}$$

where $c$ is the wavespeed. The functions $\mathscr{B}(\Psi)$ and $\mathscr{Z}(\Psi)$ are arbitrary, although together with the streamfunction $\Phi(x - ct)$, they must still satisfy the consistency condition (2.17). Here we solve the defect system numerically as a (nonlinear) initial-value problem (§ 4), extracting the form of $\mathscr{Z}(\Psi)$ and $\mathscr{B}(\Psi)$ for any nonlinear waves that emerge. Before doing that, we summarize the linear stability theory of the defects.

## 3. Linear stability theory for inviscid, non-diffusive defect

For $\nu = \kappa = 0$, the defect system (2.19)–(2.17) admits steady, horizontally homogeneous equilibria with profiles of vorticity and buoyancy given by $Z = F(\eta)$ and $B = G(\eta)$. Specific examples of basic defect profiles, $F(\eta)$ and $G(\eta)$, are shown in figure 2; our chief interest is in the instabilities suffered by the corresponding equilibrium states.

To study linear perturbations about the equilibria with the normal mode form, we set

$$\Phi = a\mathrm{e}^{\mathrm{i}k(x-ct)}, \quad Z = F(\eta) + z(\eta)\mathrm{e}^{\mathrm{i}k(x-ct)}, \quad B = G(\eta) + \beta(\eta)\mathrm{e}^{\mathrm{i}k(x-ct)}, \tag{3.1}$$

where the horizontal wavenumber $k$ is integral for our periodic domain, and the (complex) wavespeed is $c = c_r + \mathrm{i}c_\mathrm{i}$. The infinitesimal amplitudes, $a$, $z(\eta)$ and $\beta(\eta)$ are

related by the linearizations of (2.19) and (2.20):

$$z = -\frac{aF_\eta}{\eta - c} - \frac{aN^2}{(\eta - c)^2}, \quad \beta = -\frac{aN^2}{\eta - c}, \tag{3.2}$$

where $N^2 = G_\eta$ is the square of the (dimensionless) defect buoyancy frequency, $N$. The introduction of these relations into (2.17) furnishes $\Phi_n = a\delta_{kn}$ and the dispersion relation,

$$0 = D(c) := 2k - \int_{-\infty}^{\infty} \left[\frac{F_\eta}{\eta - c} + \frac{N^2}{(\eta - c)^2}\right] \mathrm{d}\eta \equiv 2k - \int_{-\infty}^{\infty} \frac{(F + N^2)}{(\eta - c)^2}\, \mathrm{d}\eta. \tag{3.3}$$

The dispersion function $D(c)$ in (3.3) is a straightforward generalization of that for unstratified defects, and the technology summarized by Balmforth *et al.* (1997) for extracting general features of the stability problem can be immediately carried over to the current problem; the stability criteria that previously hinged on the form of $F(\eta)$ (including necessary and sufficient conditions for instability), now rely on the combination $F + N^2 \equiv F + G_\eta$ (i.e. the equilibrium distribution of $\mathscr{Z}$).

### 3.1. *Symmetrical Kelvin–Helmholtz and Holmboe instabilities*

For a defect version of the equilibrium profiles suffering the classical combination of KH and Holmboe instability (i.e. the piecewise linear profiles considered originally by Holmboe 1962, or the more recent smooth profiles considered by Alexakis 2005) we adopt

$$F = \tfrac{1}{2} f[\Theta(\eta - 1) - \Theta(\eta + 1)], \quad G = \tfrac{1}{2}\gamma\Theta(\eta), \tag{3.4}$$

where the step-like function $\Theta(\eta)$ is given by either

$$\Theta(\eta) = \mathrm{sgn}(\eta), \tag{3.5}$$

or the smoothed relatives,

$$\Theta(\eta) = \frac{2}{\pi}\tan^{-1}\left(\frac{\eta}{\delta}\right) \tag{3.6}$$

and

$$\Theta(\eta) = \tanh\left(\frac{\eta}{\delta}\right). \tag{3.7}$$

Here, $f$ and $\gamma$ measure the strength of the vorticity defect and its stratification, and $\delta$ is the characteristic distance over which the discontinuity of (3.5) is smoothed by either (3.6) or (3.7); see figure 2(*a*). Note that, according to the non-dimensionalization in (2.4)–(2.5), $B_\eta \equiv L^2\hat{b}_{\hat{y}}/(\epsilon U^2)$. Therefore, $\gamma = Ri_b/\epsilon$ can be interpreted as a scaled relative of a bulk Richardson number, $Ri_b$, comparing the characteristic buoyancy frequency inside the defect to the background shear (the defect vorticity is order $\epsilon$ smaller). Given that $\gamma$ is assumed order one, this emphasizes how the bulk Richardson number is relatively small in the defect theory.

Both (3.5) and (3.6) lead to convenient analytical results; the velocity and density profiles corresponding to (3.5) take the form of 'broken lines' (with Dirac delta-functions for $F_\eta$ and $N^2$), whereas (3.6) leads to a Lorentzian form for $F_\eta$ and $N^2$. The third case in (3.7) is less analytically accessible in the linear stability theory (the integral in the dispersion relation can be expressed in terms of polygamma functions but is not particularly transparent), but is superior to the Lorentzian profiles (3.6) for nonlinear computations because of the faster decay outside the defect.

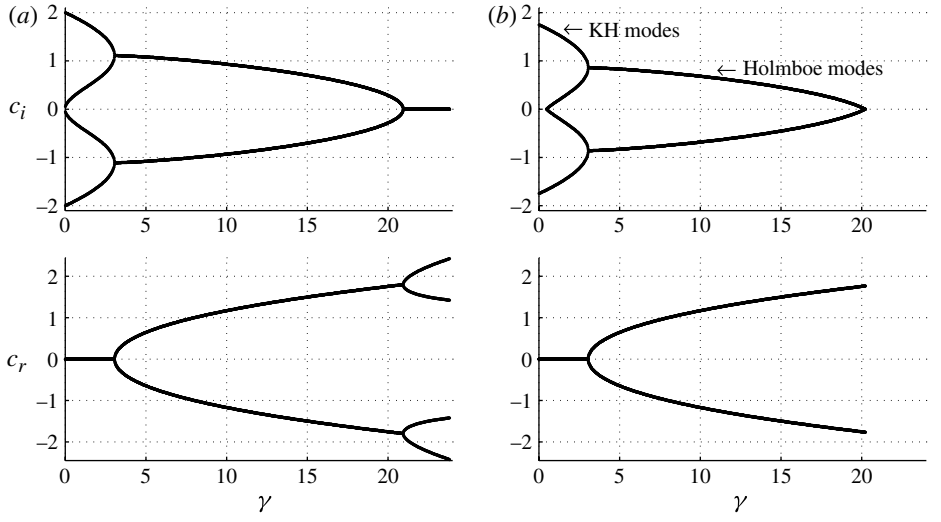


FIGURE 3. Eigenvalues of the symmetrical KH–Holmboe problem for (*a*) the broken-line profiles (3.5) and (*b*) the Lorentzian profiles (3.6), plotted against $\gamma$ for $k = 1$, $f = 2$ and $\delta = 0.25$. In (*b*), modes disappear when $\gamma = \gamma_c$, as given by (3.10), or for $\gamma = 2\delta^2(f - k - k\delta^2)/(1 + \delta^2)$. In both cases, modes with purely imaginary $c$ combine into complex pairs for the value of $\gamma$ given by (3.9).

For the broken-line profiles (3.5), the integral in the dispersion relation can be integrated to yield

$$C^4 - \left(1 - \frac{f}{k} + \frac{\gamma}{2k}\right) C^2 + \frac{\gamma}{2k} = 0, \tag{3.8}$$

where $C \equiv c$. Thus, there are four solutions for $c$ for all choices of the parameters; these modes can be complex provided that $\gamma$ is not too large, implying instability. If the phase speed, $c_r$, is zero, the unstable modes are commonly referred to as having Kelvin–Helmholtz character, but if $c_r \neq 0$ they are referred to as Holmboe instabilities. We will also use this classification, although it is not completely definitive near the parameter settings where the phase speed first becomes finite (Carpenter *et al.* 2010*a*), which can be shown to occur for

$$\gamma = 2k\left(\sqrt{\frac{f}{k}} - 1\right)^2. \tag{3.9}$$

For the Lorentzians (3.6), the integral again can be evaluated to furnish (3.8), but this time with $C = c + \mathrm{i}\delta\,\mathrm{sgn}(c_i)$, reflecting how the integral of the dispersion relation in (3.3) is not, in general, an analytic function of $c$. The origin of the non-analyticity is the continuous spectrum of singular eigenmodes that exists for all real values of $c$. The presence of $\mathrm{sgn}(c_i)$ in (3.8) generates inconsistent solutions for $c$ for certain ranges of the parameters; these solutions must be discarded as genuine normal modes. Despite this, the dependence of the unstable modes on the system parameters is very similar to the broken-line case: figure 3 displays sample eigenvalues for varying stratification

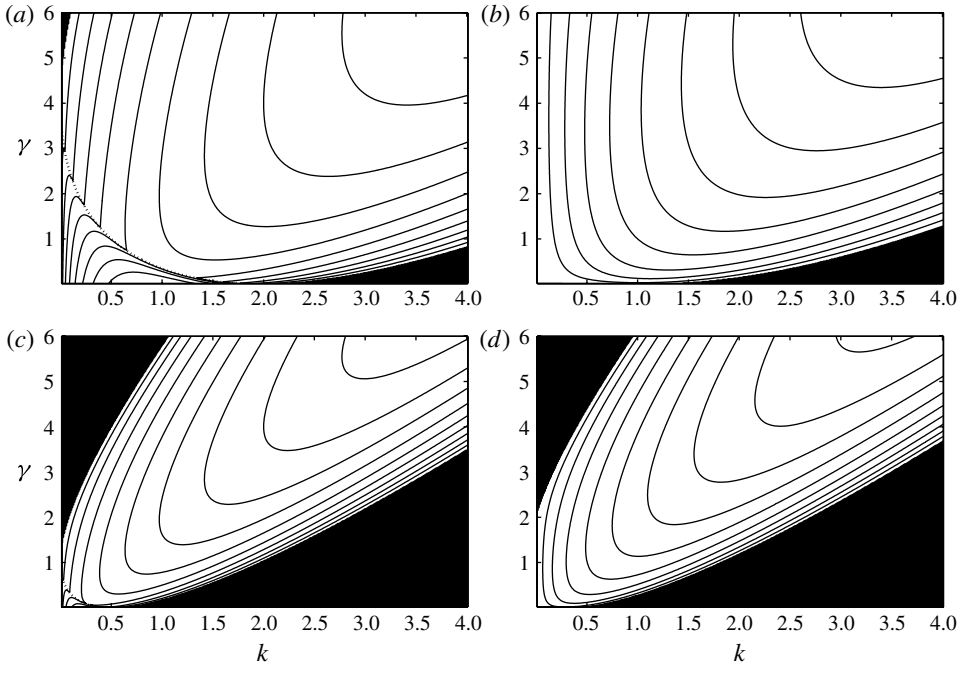


FIGURE 4. Contours of constant growth rate, $kc_i$, on the $(k, \gamma)$-plane for $(a)$ symmetrical KH/Holmboe instability and $(b)$ one-sided Holmboe instability, using Lorentzian profiles, $f = 2$ and $\delta = 0.1$. The dotted line in $(a)$ shows (3.9). The regions shaded black are stable. The contour levels are $0.1n$, $n = 1, 2, \ldots$. $(c,d)$ Similar pictures for $f = 1/2$, $\delta = 0.05$ and contour levels of $0.05n$, $n = 1, 2, \ldots$.

strength, $\gamma$. Unstable modes exist in both cases provided that $\gamma < \gamma_c$, where

$$\gamma_c = 2k\left(\sqrt{\frac{f}{k} - 4\delta^2} + 1\right)^2, \tag{3.10}$$

and

$$c_r = \pm\sqrt{\frac{1}{2}\left(1 - \frac{f}{k} + \frac{\gamma}{2k}\right) + \delta^2} \tag{3.11}$$

is the corresponding phase speed, with $\delta = 0$ providing the broken-line result. The main difference between the broken-line and Lorentzian cases arises when the normal modes intersect the continuum and $c_r \to 0$. For the former, the modes combine into neutrally stable, propagating waves. For the Lorentzian, the neutral modes merge with the continuous spectrum and cease to exist as regular discrete eigenmodes.

Figure 4 presents results in which we also vary the wavenumber $k$. Although $k$ is an integer for our periodic defect, the results in figure 4 interpolate between those digits in order to display growth rate as a continuous function over the $(k, \gamma)$-plane. In this way, we reveal the many similarities between the predictions of the defect model and the classical solutions of the Taylor–Goldstein equation (e.g. Carpenter *et al.* 2010*a*).

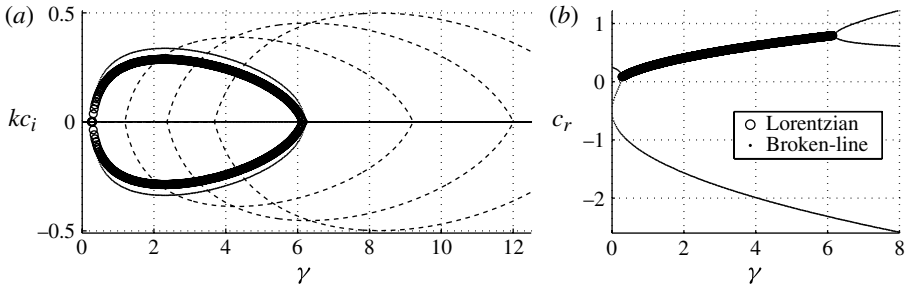


FIGURE 5. Eigenvalues for the one-sided Holmboe example (3.12) with the broken-line profiles (3.5), and the Lorentzian profiles (3.6), plotted against $\gamma$ for $k = 1$, $f = 1/2$ and $\delta = 0.05$. The dashed lines in ($a$) shows the Lorentzian growth rates for $k = 2$, 3 and 4.

### 3.2. *One-sided Holmboe instability*

As noted by Baines & Mitsudera (1994), the KH instability can be suppressed by removing one of the vorticity jumps. To consider this case, we consider the equilibrium vorticity and buoyancy profiles,

$$F = \tfrac{1}{2} f \Theta(\eta - \tfrac{1}{2}), \quad G = \tfrac{1}{2}\gamma\Theta(\eta + \tfrac{1}{2}), \tag{3.12}$$

with $\Theta(\eta)$ again given by (3.5)–(3.7). Once more, $\gamma$ is interpretable as a scaled bulk Richardson number.

For the broken-line and Lorentzian profiles, the dispersion relation takes the form:

$$\left(C + \frac{1}{2}\right)^3 + \left(\frac{f}{2k} - 1\right)\left(C + \frac{1}{2}\right)^2 - \frac{\gamma}{2k}C + \frac{\gamma}{4k} = 0. \tag{3.13}$$

As illustrated in figure 5, these profiles support a single modal Holmboe instability (see also the comparison in figure 4). Again, the unstable and decaying mode pairs are similar for both problems, but the neutrally stable propagating waves of the broken-line profile have no analogue for the Lorentzians.

### 3.3. *Taylor instability*

For the Taylor instability, we remove the mean vorticity entirely and introduce a two-step buoyancy profile:

$$F = 0, \quad G = \tfrac{1}{2}\gamma[\Theta(\eta - 1) + \Theta(\eta + 1)]. \tag{3.14}$$

With the broken-line and Lorentzian profiles, the dispersion relation is

$$C^4 - \left(2 + \frac{\gamma}{k}\right)C^2 + 1 - \frac{\gamma}{k} = 0. \tag{3.15}$$

Sample eigenvalues are illustrated in figure 6; for $\gamma > k\,(1+\delta^2)^2/(1-\delta^2)$, there are unstable modes. Note that (3.15) is identical to the long-wave, low-Richardson-number limit of the dispersion relation derived for broken-line profiles (density steps) using the Taylor–Goldstein equation (Sutherland 2010); because of these inherent approximations, the defect theory does not capture any large-stratification cut-off to the instability.

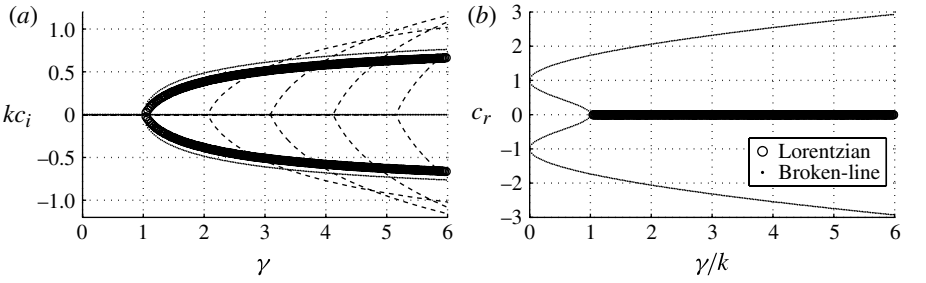


FIGURE 6. Eigenvalues for the Taylor example (3.14) with the broken-line profiles (3.5) and the Lorentzian profiles (3.6), plotted against $\gamma$ or $\gamma/k$ for $\delta = 0.1$. In (*a*) the dashed lines show the growth rates for modes with $k = 2, 3, 4$ and 5.

## 4. The nonlinear initial-value problem

We now solve the defect system (2.17)–(2.21) numerically as an initial-value problem. For the defect vorticity and buoyancy, we begin from the initial conditions,

$$Z(x, \eta, 0) = F(\eta) \quad \text{and} \quad B(x, \eta, 0) = G(\eta), \tag{4.1}$$

where $F$ and $G$ denote one of the equilibrium states explored in the previous section, defined by (3.4), (3.12) or (3.14). The states are parameterized by $f$ (measuring the strength of the vorticity defect), $\gamma$ (a scaled bulk Richardson number) and $\delta$ (the interface thickness).

To kick the system into action, we typically add a small forcing term to the vorticity–streamfunction relation in (2.17), so that

$$\Phi_n = \varepsilon_0 t \mathrm{e}^{-10t^2} \delta_{n1} - \frac{1}{2|n|} \int_{-\infty}^{\infty} Z_n(\eta, t)\, \mathrm{d}\eta, \tag{4.2}$$

where $Z_n(\eta, t)$ denotes the $n$th Fourier mode amplitudes of $Z(x, \eta, t)$, and $\varepsilon_0$ is a small forcing amplitude, typically chosen to be $10^{-2}$. As a measure of the amplitude of the modal instability, we use

$$a(t) = \left| \int_0^{2\pi} \Phi^2 \frac{\mathrm{d}x}{4\pi} \right|^{1/2}. \tag{4.3}$$

For the computations, we first discretize the spatial coordinates on the truncated domain, $0 \leqslant x \leqslant 2\pi$ and $-\eta_0 \leqslant \eta \leqslant \eta_0$, where $\eta_0$ is chosen to be sufficiently large that the location of those edges plays little role in the dynamics. We then time step the system using an algorithm based on the operator-splitting scheme of Cheng & Knorr (1976), which breaks the advection problem into two stages. Advection in $x$ is accomplished along each horizontal grid level using a Fourier series decomposition of $Z(x, \eta, t)$ and $B(x, \eta, t)$. To perform the advection in $\eta$, we fit splines to $Z(x, \eta, t)$ for each vertical grid line, then compute an approximation to $\int_{-\infty}^{\infty} Z(x, \eta, t)$ and therefore $\Phi(x, t)$. That streamfunction is unchanged by any shift of $\eta$ (as demonstrated by a change of integration variable), fixing the amount of vertical advection. The spline interpolation is then used to place the advected solution back on to the original grid points in $\eta$, with any material advected into the domain from either above or below assumed to arrive with $Z = F(\eta)$ and $B = G(\eta)$.

For our defect model, it is necessary to modify the Cheng & Knorr scheme in order to incorporate the baroclinic generation of vorticity (the right-hand side of (2.19)) and

diffusion. We include the former by modifying the advection-in-$x$ step to

$$Z_t + \eta Z_x = B_x \quad \text{and} \quad B_t + \eta B_x = 0, \tag{4.4}$$

for which we may write the explicit solution,

$$Z = Z_0(x - \eta t, \eta) + tB_{0x}(x - \eta t, \eta) \quad \text{and} \quad B = B_0(x - \eta t, \eta), \tag{4.5}$$

where $Z_0(x, \eta)$ and $B_0(x, \eta)$ denote the initial fields at the beginning of that step. To include the diffusion, we simply add an explicit diffusion step after the vertical advection using centred differences in $\eta$. We also control the time step, $\tau$, such that vertical advection never spans more than one grid interval, and by imposing a maximum step of $5 \times 10^{-3}$ or less. Given the resolutions used, we estimate that numerical smoothing becomes as large as explicit diffusion for $\nu$ and $\kappa$ of order $10^{-7}$–$10^{-8}$.

### 4.1. *Nonlinear KH dynamics*

Figure 7 shows a sample computation with $\nu = 3\kappa = 10^{-3}$ for a stratified KH instability. The pictures show the mode amplitude, $a(t)$, together with snapshots of the vorticity, $Z(x, \eta, t)$, and buoyancy, $B(x, \eta, t)$, at the selection of times indicated. The early evolution of the amplitude $a(t)$ is compared with the expected linear growth in the first panel; once the linear phase of evolution ends, the amplitude oscillates due to pulsations of the cat's eyes originating from elliptical deformations of the associated vortices. The pulsations decay slowly under the action of diffusion, with a smoothed, mixed region emerging around the eyelids of the cat's eye. Within the core of the cat's eye, a very slowly decaying coherent structure persists over times exceeding the length of the computation (which ran to $t = 100$). These observations match previous results extracted from numerical solution of the Boussinesq fluid equations and, for the later times at least, are artifacts of our two-dimensional computations (e.g. Caulfield & Peltier 2000).

Figure 7 also includes the mode amplitude for a computation with $\nu = \kappa = 10^{-3}$, which is largely identical to the original case, with $\nu = 3\kappa = 10^{-3}$, until $t \approx 30$ whereafter the increased diffusion in the density field more effectively damps the pulsation of the cat's eye. For the second computation, by $t = 60$, the oscillations in $a(t)$ associated with the cat's eye pulsations have largely died out, leaving a quasisteady, slowly diffusing state. In appendix A, we present asymptotic arguments for $\nu = \kappa$ to suggest a reduction of the defect equations in the long-time limit; unlike in a number of other shear-flow problems (e.g. Brown & Stewartson 1978; Churilov & Shukhman 1996), however, it does not seem possible to build the final state in any analytical fashion.

Figure 8 shows the final horizontal averages of the vorticity and buoyancy field for the computation of figure 7. Also shown is the final average of $\mathscr{Z} = Z + B_\eta$ for the example with $\nu = \kappa$, along with a plot of $\mathscr{Z}$ against total streamfunction, $\Psi$, for all points on the computational grid. The $(\Psi, \mathscr{Z})$-relation is largely a single function, as expected for a quasisteady state (§ 2.3). However, the relationship does not collapse completely for the highest values of $\Psi$ due to the persistence of a weak coherent structure in the core of the cat's eye, even though it is hardly discernible in the final snapshot of $\mathscr{Z}$.

Details of the transition to KH instability are illustrated in figure 9. When $\gamma = 0.2$ and $\delta = 1$, the $\nu = \kappa = 0$ instability can be triggered by raising $f$ (the strength of the vorticity defect) through its critical value, $f = f_c \approx 1.302$, exploiting the smoothing of the interfaces to avoid any Holmboe instability (with sharper interfaces, instability

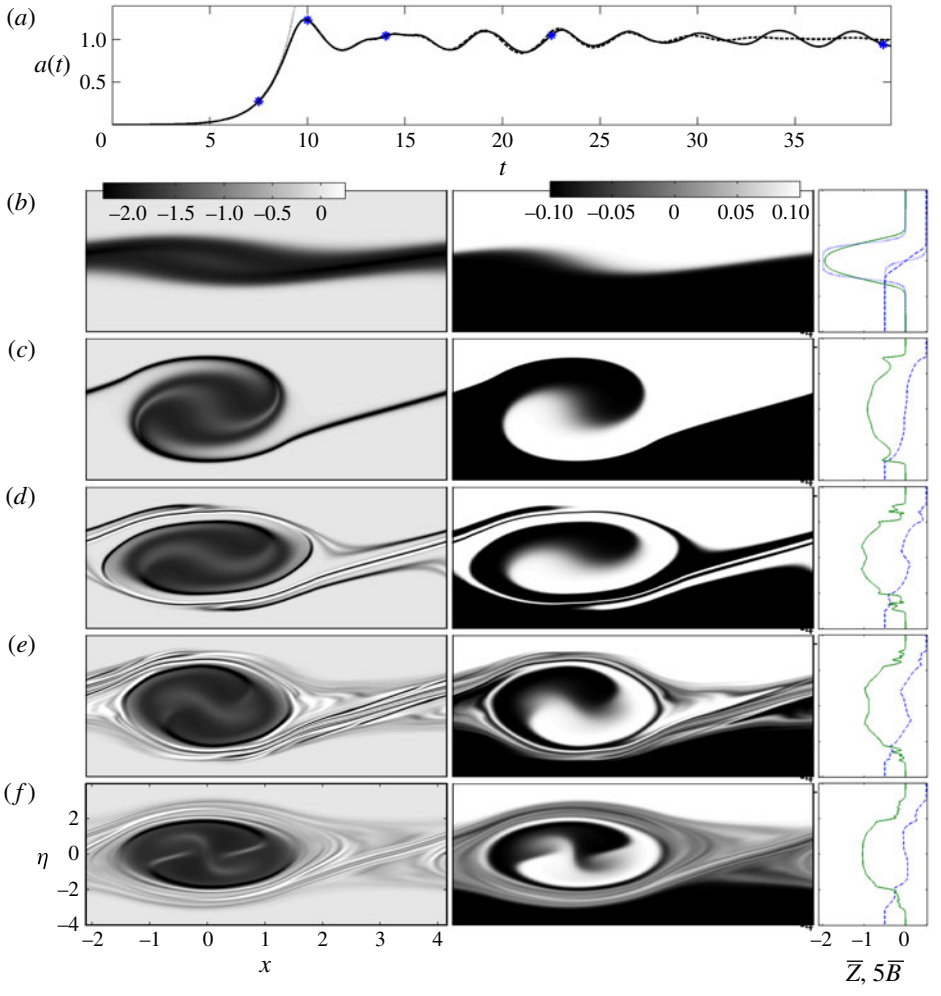


FIGURE 7. (Colour online available at journals.cambridge.org/flm) Numerical solution of the KH instability for (3.4), (3.7) and (4.1)–(4.2) with $f = 2$, $\gamma = 0.2$, $\delta = 1/4$ and $\nu = 3\kappa = 10^{-3}$. The top panel shows a time series of the mode amplitude, $a(t)$, along with the expected linear growth (dotted line). The dashed line shows $a(t)$ for the $\nu = \kappa = 10^{-3}$ reduced system in (2.23). The stars mark the instants at which snapshots of vorticity, $Z$, and buoyancy, $B$, are shown in the series of plots underneath, with $Z$ on the left and $B$ on the right (the computational domain used is larger than the region shown in order to illustrate the main features of the dynamics, a device used in all of the results presented below). The plots on the right-hand side show the horizontal averages of $Z$ (solid lines) and $B$ (dashed lines).

first appears through Holmboe waves on varying $f$). Beyond onset, the strength of the emerging cat's eye patterns increases smoothly, as can be quantified by recording the amplitude of the first maximum in $a(t)$ (after initial transients have subsided and the system has locked onto the exponentially growing linear mode; see figure 9*a*). This saturation measure, $a_*$, is plotted against $f - f_c$ in figure 9(*b*). Just beyond onset for $\nu = \kappa = 10^{-8}$, we observe that $a_* \sim (f - f_c)^2$, which is the 'trapping scaling' of O'Neil, Winfrey & Malmberg (1971) found for the Vlasov problem, and consistent with the critical-layer theory of Churilov & Shukhman (1987) and others (e.g. Balmforth,

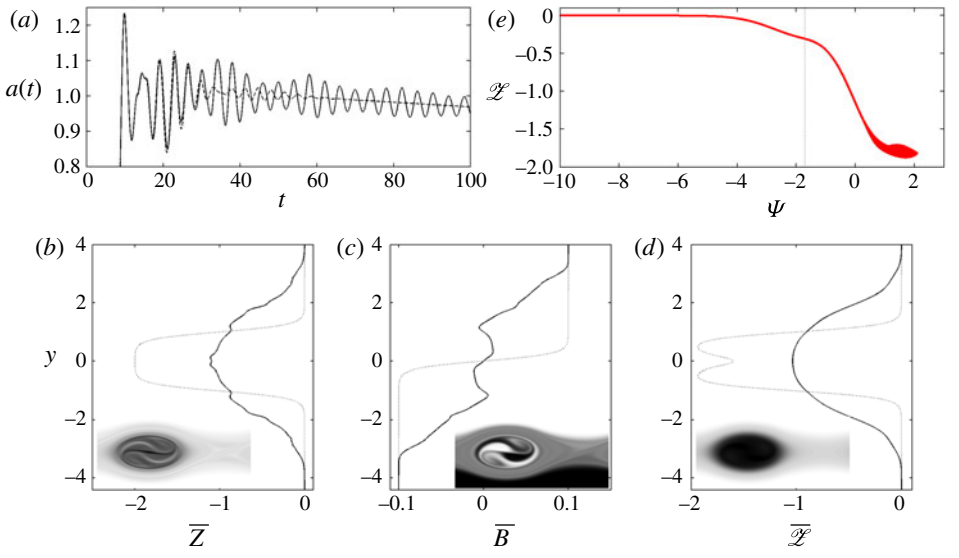


FIGURE 8. (Colour online) Longer-time details of the two computations shown in figure 7. (*a*) Two extended time series of $a(t)$. (*b,c*) The final ($t = 100$) horizontal averages (solid line) of $Z$ and $B$ for the computation with $\nu = 3\kappa$, together with the initial conditions (dotted line). (*d*) The initial (dotted line) and final (solid line) horizontal average of $\mathscr{Z} = Z + B_\eta$ and $\nu = \kappa$. The insets of (*b–d*) show the final snapshots of $Z$, $B$ and $\mathscr{Z}$. (*e*) The corresponding $(\Psi, \mathscr{Z})$-relation; the vertical dotted line indicates the cat's eyelid.

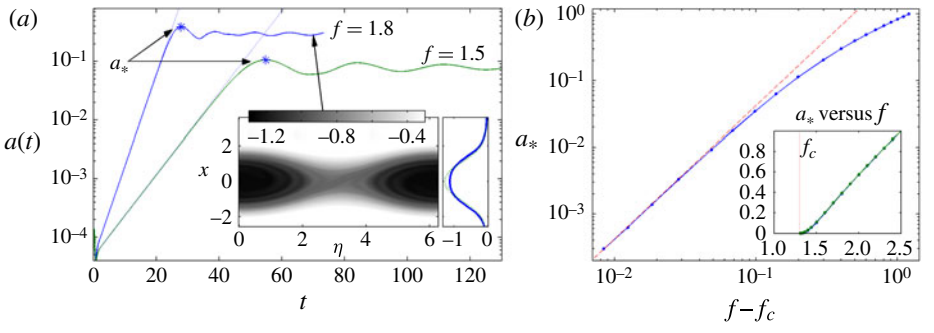


FIGURE 9. (Colour online) (*a*) Mode amplitudes for $f = 1.5$ and 1.8, showing the definition of $a_*$, and (*b*) scaling data, $a_*$ against $f - f_c$, for KH instabilities with $\nu = \kappa = 10^{-8}$, $\gamma = 0.2$ and $\delta = 1$. In (*a*), the dotted lines show the expected linear growth and the inset shows a snapshot of $\mathscr{Z} = Z + B_\eta$ with $f = 1.8$ at $t = 70$, with the plot to the right indicating the $x$-average (solid lines) and the equilibrium profile (dotted lines). The dashed line in (*b*) shows the prediction of the single-wave model; the inset shows $a_*$ against $f$, with the threshold, $f = f_c$, indicated by the vertical dotted line.

Morrison & Thiffeault 2012). Asymptotic reduction in this regime furnishes another reduced description, the 'single-wave model', which crucially removes singularities from the critical levels of weakly unstable modes (see Balmforth *et al.* 2012). The prediction of the single-wave model is also indicated in figure 9(*b*) (i.e. the scaling factor in $a_* \propto (f - f_c)^2$; equation (B 17)). Note that these results partly reflect the choice $\nu = \kappa \ll 1$: as shown by Shukhman & Churilov (1997), stronger diffusion

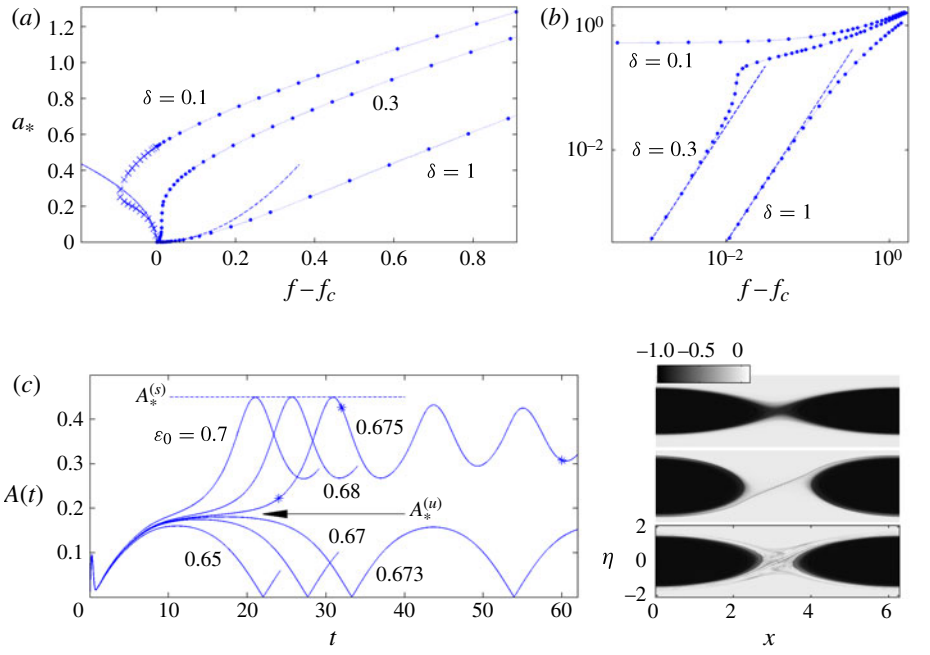


FIGURE 10. (Colour online) First maximum of the mode amplitude, $a_*$, against $f$ plotted (*a*) on a linear graph and (*b*) logarithmically, for KH instabilities of unstratified defects with $\nu = \kappa = 10^{-8}$, $\varepsilon_0 = 10^{-3}$ and three values of the interface sharpness parameter, $\delta$ (as indicated). In (*a*), the unstable, weakly nonlinear equilibrium, $a_* = \sqrt{f_c - f}$, of the broken-line case (appendix B) is shown by the solid line. The dashed lines show the predictions of the single-wave model. In (*c*), with $f < f_c$ and $\delta = 0.1$, we plot mode amplitudes for a suite of initial-value problems with different forcing amplitude, $\varepsilon_0$ (as indicated). For $\varepsilon_0 = 0.675$, the stars indicate the times of the three snapshots of $\mathscr{Z}(x, \eta, t)$ shown to the right. The 'stable' and 'unstable' first maxima, $A_*^{(s)}$ and $A_*^{(u)}$, are indicated; this data, for varying $f$, is also shown in (*a*) by the crosses.

and a different Prandtl number can change the qualitative features of the dynamics near onset.

The details of the transition also critically depend on the smoothness of the interfaces. To demonstrate this, we focus on the unstratified problem to eliminate the Holmboe instability altogether. Figure 10 shows the saturation measure, $a_*$, against $f - f_c$ for three values of $\delta$, the interface sharpness parameter. For the case with the broadest interfaces ($\delta = 1$), the transition is again relatively smooth and characterized by the trapping scaling. The case with the sharpest interfaces ($\delta = 0.1$), however, is quite different, with $a_*$ jumping discontinuously from zero to finite values at the linear stability threshold (see figure 10*b*). The intermediate case, with $\delta = 0.3$, combines an initial smooth onset following the trapping scaling with a subsequent sharp increase in amplitude (although the solution branch remains continuous).

Thus, the transition is much more abrupt if the interfaces are sufficiently sharp. In fact, in the limit $\delta \to 0$, corresponding to broken-line equilibria, the single-wave model does not describe the onset of instability because the unstable modes no longer suffer critical-level singularities; instead, the weakly nonlinear description is a standard one, as outlined in appendix B. That analysis indicates that the instability bifurcates

subcritically, with an unstable finite-amplitude solution existing for $f < f_c$, as drawn in figure 10(*a*).

Evidently, the abruptness of the transition for small $\delta$ is connected in some fashion to the impending subcritical bifurcation of the broken-line limit. Moreover, the finite-amplitude states reached in the initial-value problems for $f > f_c$ likely continue to lower $f$. To verify this feature numerically, and to decode the dynamics below the linear instability threshold, we perform initial-value computations in which the equilibrium is forced with a much stronger initial kick (i.e. larger value for $\varepsilon_0$ in (4.2)). For $f < f_c$, the initial-value problems display a clear threshold behaviour with varying $\varepsilon_0$ (figure 10*c*): sufficiently strong forcings, $\varepsilon_0$, trigger a growth of the mode amplitude up to a level, $A_*^{(s)}$, that is otherwise independent of $\varepsilon_0$. The system subsequently develops a pulsating cat's eye pattern much like the states generated in the linearly unstable regime. Below the forcing threshold, on the other hand, the system executes regular, weakly decaying oscillations with an amplitude set by $\varepsilon_0$, and $\mathscr{Z}(x, \eta, t)$ develops no persistent pattern. The threshold forcing amplitude corresponds to a first maximum, $A_*^{(u)}$ that we identify as evidence of an unstable nonlinear state. By recording the two maxima, $A_*^{(u)}$ and $A_*^{(s)}$, in suites of computations with varying $f$, we then continue the data of figure 10 to $f < f_c$; see figure 10, for $\delta = 0.1$. The data for $A_*^{(s)}$ evidently continue $a_*$ from $f > f_c$ into the linearly stable regime. This 'stable branch' of solutions terminates at lower $f$ by colliding with the 'unstable branch' characterized by $A_*^{(u)}$. The latter also converges towards the weakly nonlinear solution predicted for the broken-line profile as $f$ approaches the linear instability threshold from below.

It also turns out to be possible to trigger a transition to a finite-amplitude subcritical state by raising the amount of diffusion (for $\nu = \kappa$). We illustrate this behaviour later for the one-sided Holmboe and Taylor instabilities, whose dynamics are similarly affected by the sharpness of the interfaces and the degree of diffusion.

### 4.2. *Nonlinear Holmboe instabilities*

#### 4.2.1. *Symmetrical Holmboe instability*

Figure 11 shows a numerical computation of a symmetrical Holmboe instability. The initial kick to the system generates an unstable mode that grows until nonlinear effects arrest the instability, at which point a pair of counterpropagating nonlinear waves emerge. Simultaneously, the vorticity distribution rolls up above and below the density interface into well-defined vortices that deform the density interface, creating the cuspy features characteristic of nonlinear Holmboe waves. The beating of the two counterpropagating Holmboe waves generates regular oscillations in the streamfunction amplitude, $a(t)$, and complicates the nonlinear dynamics (cf. Smyth *et al.* 1988). Therefore, to illustrate Holmboe instability more transparently, it proves convenient to filter one of these waves by considering the one-sided problem of § 3.2.

#### 4.2.2. *One-sided Holmboe instability*

A simulation of a one-sided Holmboe instability is shown in figure 12. This time, a single wave-vortex pattern emerges, again characterized by strong filamentation of the vorticity distribution, $Z(x, \eta, t)$, and a cusped wave crest in the density field, $B(x, \eta, t)$ (at least for times before the smoothing action of diffusion takes effect). Note the strong baroclinic generation of negative vorticity below the vortex and the positive vorticity generated underneath the hyperbolic point. Also, the continued roll-up of the main vortex prompts the formation of finer-scaled features in the density field that look much like incipient Holmboe waves.

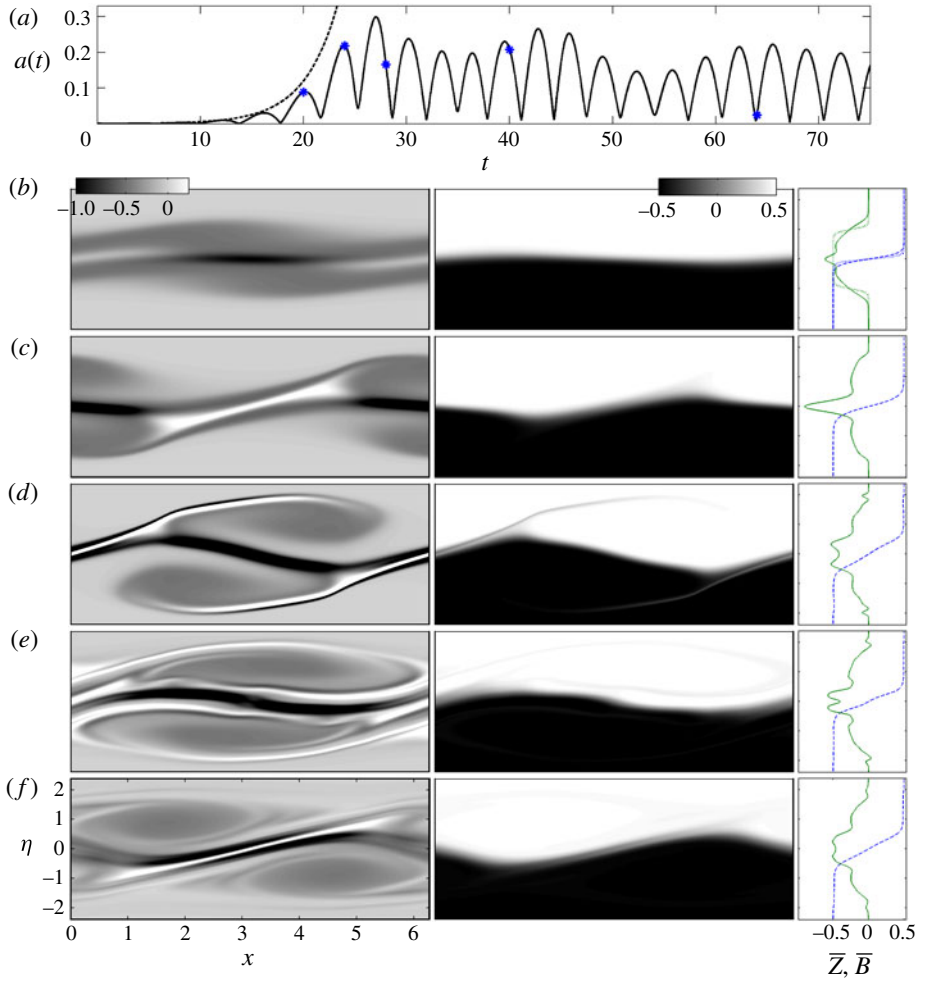


FIGURE 11. (Colour online) Numerical solution of symmetric Holmboe instability for (3.4), (3.7) and (4.1)–(4.2) with $f = 1/2$, $\gamma = 1$, $\delta = 0.1$ and $\nu = 3\kappa = 9 \times 10^{-4}$. (*a*) A time series of the mode amplitude, $a(t)$, along with the expected linear growth (dashed line). The stars mark the instants at which the snapshots of $Z$ and $B$ are shown in the series of plots in (*b–f*); the horizontal averages of $Z$ (solid lines) and $B$ (dashed lines) are shown in the right-hand plots (the dotted lines in the first plot shows the equilibrium profile).

Owing to the severe filamentation of the vorticity distribution, diffusion typically becomes significant once the instability saturates. Figure 13 illustrates further details of the effect of the dissipative parameters over longer times. Eventually, the winding up of the fluid by the instability gives way to a protracted diffusive phase. At this stage, the system relaxes to a quasisteady state with a slowly spreading nonlinear wave. The limiting $\nu = \kappa$ state is described by $\mathscr{Z} = \mathscr{Z}(\Psi)$, as illustrated in figure 13. The $(\Psi, \mathscr{Z})$-relation has three branches: $A$ describes the vortex, whereas $B$ and $C$ represent the regions below and above that cat's eye pattern, respectively. All three are connected continuously (but not particularly smoothly) across a single point of the $(\Psi, \mathscr{Z})$-relation representing the separatrices of the cat's eye.

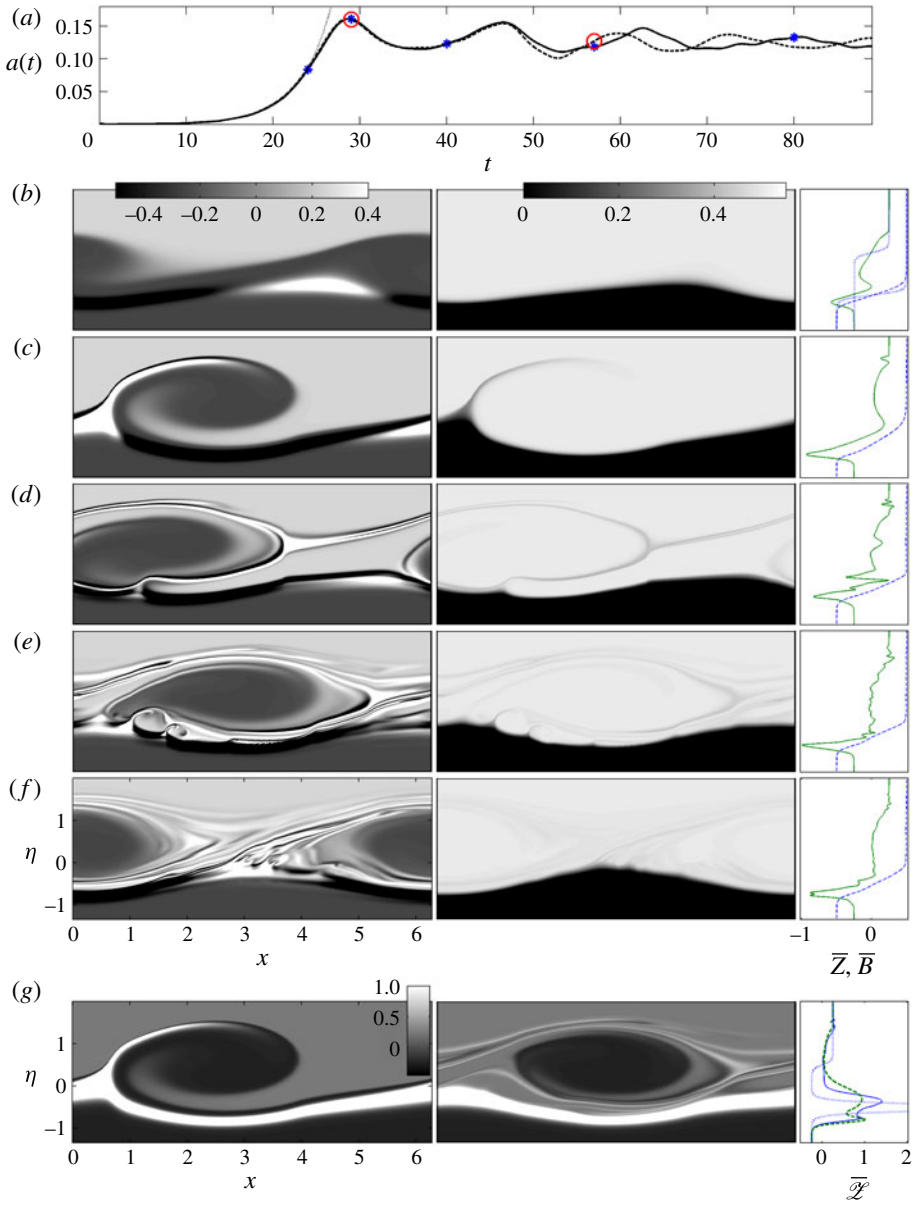


FIGURE 12. (Colour online) One-sided Holmboe instability for (3.12) and (3.7) with $f = 1/2$, $\gamma = 1$, $\delta = 0.1$ and $\nu = 3\kappa = 10^{-4}$. (*a*) A time series of $a(t)$, along with the expected linear growth (dotted line) and a second computation with $\nu = \kappa = 1/3 \times 10^{-4}$. The stars mark the instants at which the snapshots of $Z$ and $B$ are shown in the series of plots in (*b–f*), with $Z$ on the left and $B$ on the right. The plots to the right show the horizontal averages of $Z$ (solid) and $B$ (dashed) and the dotted lines in the first plot show the equilibrium profiles. The circles in (*a*) locate the times at which the $\nu = \kappa$ solution for $\mathscr{Z}$ are plotted in (*g*), with the horizontal averages (that at $t = 29$ is shown as dashed lines) and truncated initial profile (dotted lines) in the right-hand plots.

Another noteworthy point is that the solutions for larger Prandtl number, $\nu/\kappa$, display more fine-scale spatial structure than their $\nu = \kappa$ counterparts (as can be seen

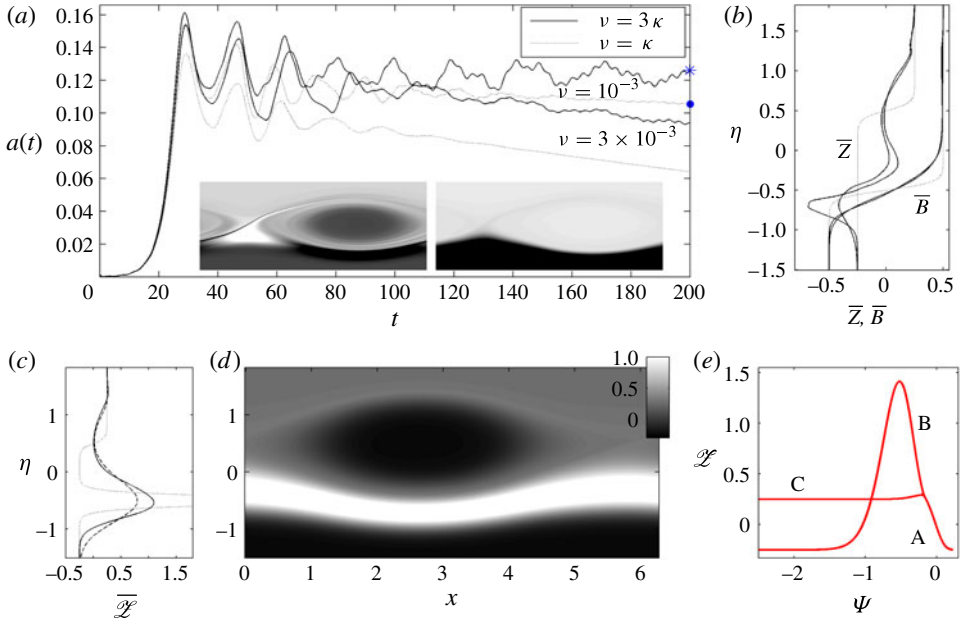


FIGURE 13. (Colour online) One-sided Holmboe instability for $f = 1/2$, $\gamma = 1$, $\delta = 0.1$ and the values of $\nu$ and $\kappa$ indicated. (*a*) shows $a(t)$; the inset is a snapshot of $Z$ and $B$ at $t = 200$ for $\nu = 3\kappa = 10^{-4}$ (marked by the star in the main panel). The final horizontal averages of $Z$ and $B$ for $\nu = \kappa$ are shown in (*b*) (the profiles are steeper for the smaller diffusion case) along with the initial conditions (dotted lines). (*c–e*) show details of the final, $\nu = \kappa = 10^{-4}$ solution (marked by the solid circle in *a*). Shown are $\overline{\mathscr{Z}}$ (the dotted line is the truncated initial condition, and the dashed line shows the final average for the computation with $\nu = \kappa = 3 \times 10^{-4}$), a snapshot of $\mathscr{Z}(x, \eta, t)$, and the $(\Psi, \mathscr{Z})$-relation (with labels indicating the main vortex, A, and the regions below and above, B and C).

by comparing equivalent snapshots in figure 12). This feature was previously noted for the KH instability by Staquet (1995), and more recently by Mashayek & Peltier (2011*a*) and Rahmani (2011), and is apparent in our solutions for all three types of instability.

4.2.3. *Onset*

To explore one-sided Holmboe dynamics near onset, we pick $f = 1/2$, $\nu = \kappa$ and $\delta = 0.1$, then vary $\gamma$ through its critical value of $\gamma_c \approx 0.228$ (cf. figure 5). We again record the first maximum of the mode amplitude, $a_*$, beyond the initial phase of linear growth as a measure the level of saturation. The trend of this measure with $\gamma$ is shown in figure 14. The onset of Holmboe waves is relatively sharp, with clear evidence for nonlinear structures existing below the linear instability threshold.

Further details of the dynamics near onset are provided in figure 15, which shows mode amplitudes for computations straddling the linear instability threshold. Figures 14 and 15 also plot growth rates, computed assuming that the equilibrium profile is fixed and does not diffuse (and employing the methods outlined by Balmforth 1998). These results demonstrate that diffusion actually destabilizes the ideal equilibria, a result that can be established more formally using the perturbation techniques outlined by Balmforth (1998). In fact, as illustrated by the mode amplitudes in figure 15(*a*), the destabilization extends to the nonlinear dynamics: after a transient

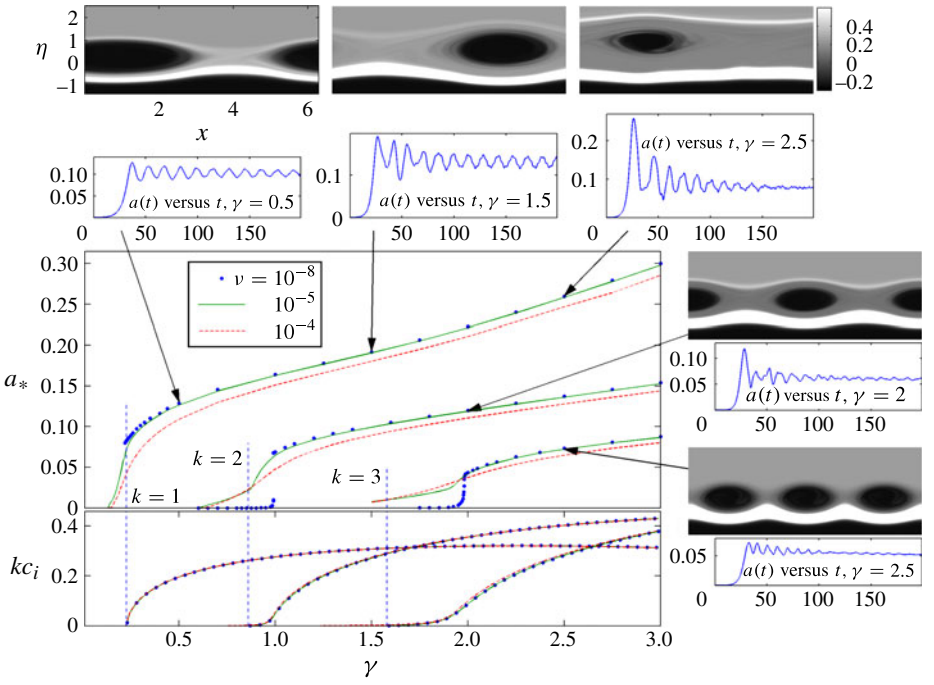


FIGURE 14. (Colour online) Scaling data for one-sided Holmboe instability. The main panel shows the first maximum of the mode amplitude, $a_*$, against $\gamma$ for $f = 1/2$, $\delta = 0.1$ and the three values of $\nu = \kappa$ indicated. Solutions in periodic domains of length $2\pi/k$ with $k = 1$, 2 and 3 are plotted. Immediately below, linear growth rates, $kc_i$, are shown for the same values of $\nu = \kappa$, computed assuming a non-diffusing equilibrium profile (the three sets of growth rates are barely distinguishable). The vertical lines indicate the linear instability thresholds for $\nu = \kappa = 0$. The adjacent panels show $a(t)$ and the final snapshots of $\mathscr{Z}(x, \eta, 200)$ for the values of $\gamma$ and $k$ indicated and $\nu = 10^{-5}$. The shading scheme is the same for each snapshot, and saturates over the main peak to emphasize the details of the cat's eyes.

in which $a(t)$ follows the growth expected for the inviscid normal modes, diffusion accelerates that growth and expedites the entrance to the nonlinear regime (although the eventual saturation of the instability is assisted by diffusion, lowering $a_*$; see figure 14). This acceleration cannot be explained by the relatively modest enhancement of the linear growth rate by diffusion indicated above. More significant is that, over the time scales on which the instability grows near onset, the background profile diffuses significantly. The viscous destabilization therefore results from the combination of diffusion of the equilibrium and the superposed instability. Importantly, as is clear from the examples with $\gamma < \gamma_c$ in figure 15(*b*), this effect carries over into the linearly stable regime, and allows modes to amplify even below the inviscid linear threshold, thereby generating subcritical nonlinear Holmboe waves (as we remarked earlier in § 4.1).

The growth rates shown earlier in figure 5 indicate that additional modes with higher horizontal wavenumber become unstable for larger $\gamma$. The nonlinear solutions that correspond to the unstable modes with $k > 1$ can be computed as for the fundamental modes ($k = 1$) by solving the initial-value problem in periodic domains of length $2\pi/k$. Figure 14 includes such results for the first and second overtones, $k = 2$ and 3. Note that the sharp increases in saturation measure coincide with similarly abrupt

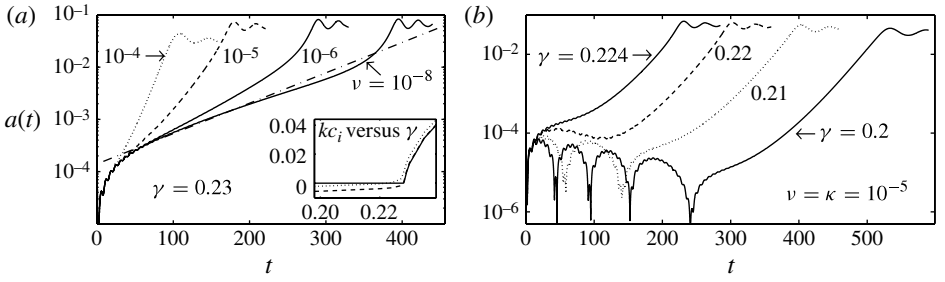


FIGURE 15. Mode amplitudes for (*a*) unstable profiles with $\gamma = 0.23$, for the four values of $\nu = \kappa$ indicated and (*b*) stable profiles for $\nu = \kappa = 10^{-5}$ and four values of $\gamma$. The dot-dashed line in (*a*) indicates the expected, inviscid linear growth, and the inset shows growth rates, $c_i$, against $\gamma$ for the same values of $\nu = \kappa$, computed assuming a fixed equilibrium profile. In all cases, $f = 1/2$, $\delta = 0.1$ and $\varepsilon_0 = 10^{-3}$.

increases in growth rate. For the fundamental mode, $k = 1$, the sharp rise in growth rate corresponds to the onset of instability. For $k = 2$ and 3, however, the rise of $kc_i$ is preceded by a shallower 'skirt', with onset occurring at somewhat smaller values of $\gamma$. Such skirts are a further consequence of the smoothing of the equilibrium interfaces; the sudden increases in growth rate are the remnant of the pure interfacial interaction. With lower diffusion, $\nu = \kappa = 10^{-8}$, the $k = 3$ solution branch appears to remain continuous, whilst there are discontinuous jumps for $k = 1$ and 2; higher diffusion smooths out all three branches.

4.2.4. *Secondary instabilities and coarsening*

Although the higher-overtone modes with $k = 2$ and 3 pictured in figure 14 are stable solutions of initial-value problems computed in domains of length $2\pi/k$, they do not remain stable when the domains are lengthened to $2\pi$. Instead, although the states can be generated initially by suitably forcing the streamfunction (replacing the $n = 1$ forcing in (4.3) by one with $n = 2$ or 3), lower wavenumbers grow unstably from low amplitude to disrupt the multiple-wave patterns. The disruption takes the form of wave mergers that coarsen the pattern, leaving a single Holmboe wave in the domain; see figure 16(*a–d*).

Coarsening dynamics is a familiar feature of the KH instability, with the celebrated 'pairing' instability increasing the vertical extent of a mixing layer (Winant & Browand 1974). However, there is a much greater variety in the form of coarsening instabilities, as noted by Klaassen & Peltier (1989) and evident in the solutions shown in figure 16. As far as we are aware, no previous studies have investigated the secondary instabilities of nonlinear Holmboe waves (or indeed the Taylor billows of § 4.3.2). In the one-sided Holmboe examples shown in figure 16, the overtones coarsen despite being more linearly unstable than the fundamental. Likewise, if the computation begins with a melange of all five unstable modes at this parameter setting ($n = 1$–5), the $n = 2$ and 3 modes outgrow the others initially, generating a state with three unequal Holmboe waves, but mergers again ensue and the fundamental still dominates eventually (see figure 16*e–f*).

The snapshots of the coarsening solutions in figure 16 are reminiscent of two-dimensional vortex dynamics. Indeed, the fluid is almost homogeneous above the density interface where the Holmboe wave vortices circulate and interact. Thus, the wave evolution is largely a manifestation of the dynamics of the associated vortices,

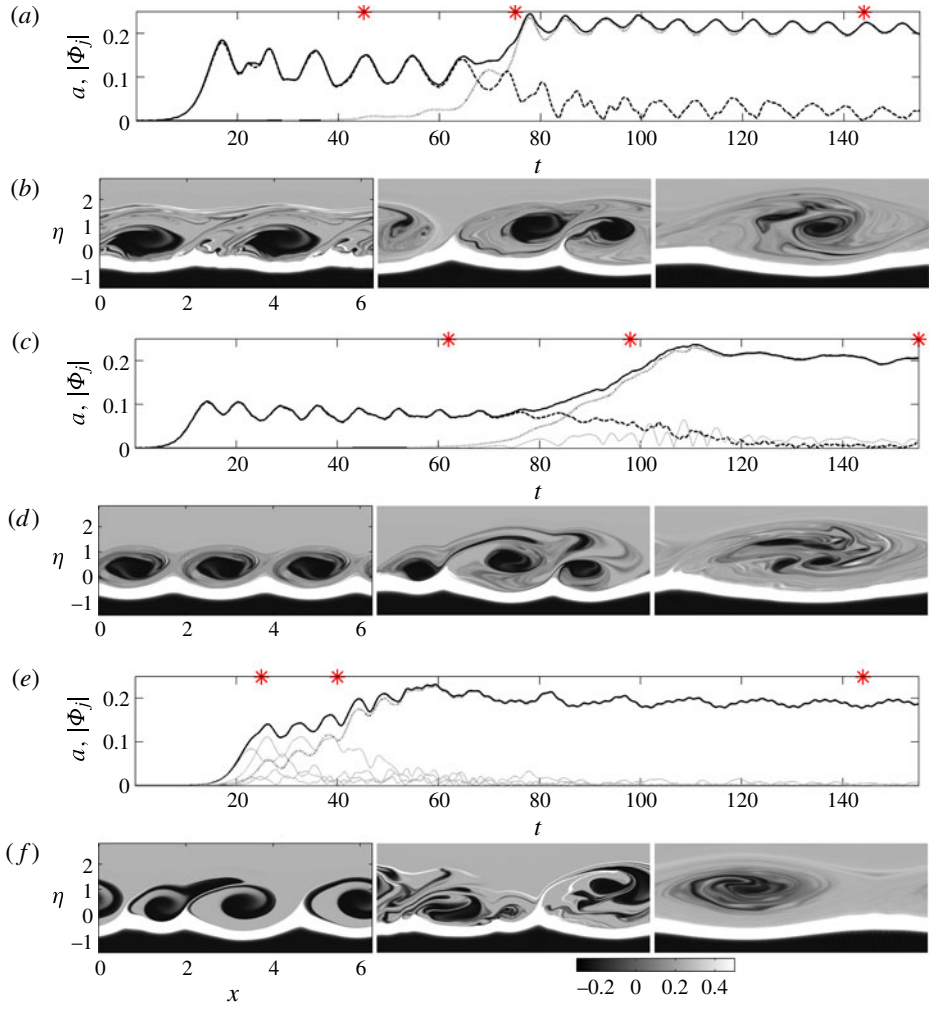


FIGURE 16. (Colour online) Coarsening computations for $f = 1/2$, $\gamma = 4$, $\delta = 0.1$ and $\nu = \kappa = 10^{-5}$, in which the streamfunction is forced by $(a,b)$ $(10^{-4}\delta_{n1} + 10^{-2}\delta_{n2})te^{-10t^2}$, $(c,d)$ $(10^{-6}\delta_{n1} + 10^{-2}\delta_{n3})te^{-10t^2}$ and $(e,f)$ $\sum_{j=1}^{5} 10^{-4}\delta_{nj}te^{-10t^2}$. $(a,c,e)$ plot $a$ (solid line) and $|\Phi_1|$ (dotted line). In $(a)$, the dominantly forced mode, $|\Phi_2|$, is shown dashed, and $|\Phi_3|$ in light grey. In $(c)$, $|\Phi_3|$ is the dominantly forced mode and shown dashed; $|\Phi_2|$ is light grey. In $(e)$, $|\Phi_n|$ for $2 \leqslant n \leqslant 5$ are shown in light grey. The stars indicates the times of the snapshots of $\mathscr{Z}$ in $(b,d,f)$ (the shading scheme is the same for all and saturates over the main peak).

illustrating how those structures are a defining characteristic of Holmboe waves. By contrast, the familiar cusp-like features of the density field are simply symptomatic of the vortices stripping material from the interface, and are not key elements in the dynamics.

As illustrated in figure 4, the $n = 1$ mode is linearly unstable for $\gamma = 4$, but a further increase of that parameter stabilizes this mode, raising the question of whether coarsening still continues to generate the fundamental wavelength at stronger stratifications. A key issue is that, in the absence of an instability with $n = 1$, there

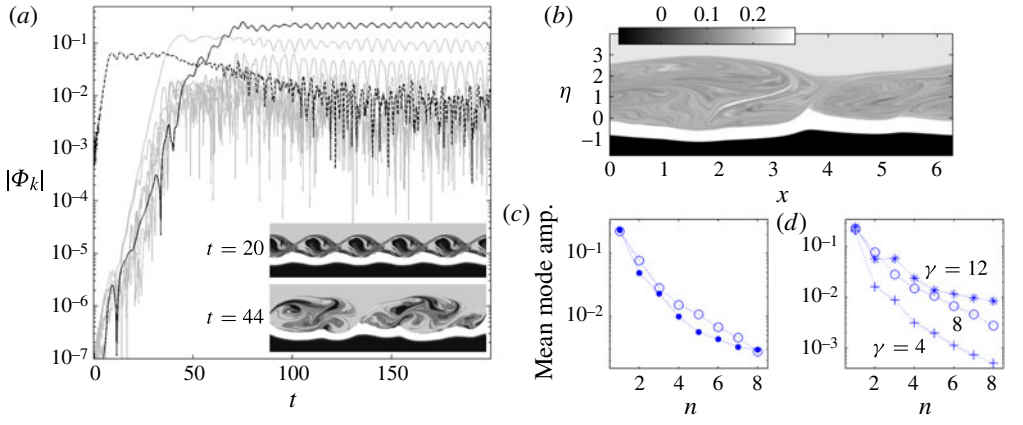


FIGURE 17. (Colour online) Coarsening computations for $f = 1/2$, $\gamma = 8$, $\delta = 0.1$ and $\nu = \kappa = 10^{-5}$, in which the streamfunction is forced initially by $(10^{-2}\delta_{n5} + 10^{-6}\sum_{j=1}^{8}\delta_{nj})te^{-10t^2}$. (*a*) The Fourier mode amplitudes, $|\Phi_n(t)|$, for $n = 1, \ldots, 8$, with the fundamental shown by the darker solid lines, the most unstable mode ($n = 5$) shown dashed, and the other modes indicated by the lighter lines. Snapshots of the wave patterns in $\mathscr{Z}$ at $t = 20$ and 44 are shown as insets. (*b*) A snapshot of $\mathscr{Z}(x, \eta, 150)$ illustrating the long-time pattern. (*c*,*d*) The mode amplitudes, $\Phi_n$, averaged over $150 < t < 200$, against $n$ (circles); in (*c*) the black dots indicate the result of a second computation in which all of the eight lowest modes are forced evenly at the outset, whereas (*d*) shows results for $\gamma = 4$ and 12 (dominantly forcing the most unstable mode at the outset, as in (*a*,*b*) and figure 16*e*,*f*).

may be no nonlinear Holmboe wave with that wavenumber to provide the coarsened end state, despite the subcritical nature of the transition to instability. In fact, we observe that the Holmboe waves still coarsen to states dominated by the fundamental mode for stronger stratifications, as illustrated in figure 17. Admittedly, with the increased stratification, the higher modes become stronger, degrading the cat's eye pattern and enriching the Fourier mode spectrum (see figure 17*c*–*d*). Nevertheless, other considerations suggest that it is dangerous to conclude that the one-sided Holmboe instability always generates a solution dominated by the gravest wavelength via an inverse cascade: the deformation of the density interface by the vortices implies an energetic cost that might, at yet higher $\gamma$, penalize coarsening sufficiently to arrest the process over intermediate length scales.

We have also observed a different type of secondary instability for stronger vorticity interfaces and larger Prandtl numbers: for larger $f$, the Holmboe instabilities have an enhanced effect on the density field, with the main vortex more strongly filamenting the density field (see figure 18). Despite this, the nonlinear Holmboe wave that first emerges has qualitative features that mirror the solutions presented earlier. Somewhat later, however, the mode amplitude develops beating oscillations. We trace these to the growth of a counterpropagating wave riding on the residual density interface (see the final two snapshots in figure 18). Associated with the secondary wave is a conspicuous vortex lying beneath the density interface that strips off lighter overlying fluid, entraining that material below and deforming the density interface into a cuspy form. This structure leads us to identify the secondary instability as another Holmboe wave, growing parasitically atop the primary wave.

It is important to stress that the secondary instabilities detected above are purely two-dimensional. As already noted in the introduction, for flow subject to

KH instability, the two-dimensional subharmonic merging (or 'pairing') instability can coexist with inherently three-dimensional instabilities. Furthermore, in certain parameter regimes (particularly at higher Reynolds number, see Mashayek & Peltier 2011*b* for a fuller discussion), the small-scale two-dimensional secondary shear instability predicted by Corcos & Sherman (1976) can also be observed to reach finite amplitude in the braid between neighbouring KH billow cores, even in the presence of a range of inherently three-dimensional secondary instabilities. Therefore, we believe that it is worthwhile to catalogue the two-dimensional secondary instabilities in view of the possibility that they may appear in three-dimensional flow for some ranges of physical parameters, competing with three-dimensional secondary instabilities as the flow undergoes a transition to turbulence.

### 4.3. *The nonlinear dynamics of Taylor's instability*

#### 4.3.1. *The billows*

An example of our third instability is displayed in figure 19. In this case, the linear instability perturbs the two density interfaces towards one another, baroclinically generating a signature in the vorticity field. The continued growth of the unstable mode causes the intermediate layer to pinch off and contract into an elliptical patch, or 'billow', of roughly constant density. The billow becomes shrouded by sharp filaments of vorticity and begins to pulsate somewhat like the cat's eyes of the KH instability. These features mirror previous experimental and numerical observations (Caulfield *et al.* 1995; Lee & Caulfield 2001).

Over longer times, the baroclinically generated vortex filaments become increasingly wound up around the elliptical patch; for higher Prandtl number, the filaments suffer secondary instability, rolling up to generate significant fine structure (see figure 19*f*). For a lower Prandtl number ($\nu = \kappa = 3.33 \times 10^{-4}$), the solution remains smoother, and after a sufficiently long time, develops into a slowly decaying nonlinear wave. Details of this solution, including its ($\Psi$, $\mathscr{Z}$)-relation, are illustrated in figure 20.

As illustrated in § 3.3, the Taylor instability can be generated by fixing the interface thickness ($\delta$) and then raising the stratification parameter, $\gamma$, through the threshold, $\gamma = \gamma_c \approx k$ (for small $\delta$, $\nu$ and $\kappa$). Once more, we track how the instability develops in the vicinity of this onset by performing suites of initial-value problems with varying $\gamma$. Saturation measures, $a_*$, are plotted against $\gamma$ in figure 21, for three cases with the values of $\nu = \kappa$ and $\delta$ indicated. As found for the other instabilities, the smoother profiles display a gradual onset following the trapping scaling, whereas sharper interfaces lead to a sudden transition that can be smoothed and extended below the linear instability threshold by diffusion. For less diffusion, the nonlinear states bifurcate subcritically (see also the broken-line calculation in appendix B), then turn around at smaller $\gamma$.

#### 4.3.2. *Coarsening and other secondary instabilities*

For larger $\gamma$, Taylor modes with higher horizontal wavenumber also become unstable (cf. figure 6), highlighting the existence of further billow solutions. The solutions with $k > 1$ can again be tracked by performing computations in periodic domains of length $2\pi/k$; the corresponding saturation measures for $k = 2$ and 3 are compared with the fundamental solution branch ($k = 1$) in figure 22(*a*).

Similarly to the one-sided Holmboe waves, if the $k = 2$ and $k = 3$ nonlinear states are generated by suitably forcing the corresponding Fourier modes of the streamfunction in periodic domains of length $2\pi$, they do not remain stable: as illustrated by the two computations of figure 22 with $k = 2$ and 3, these structures

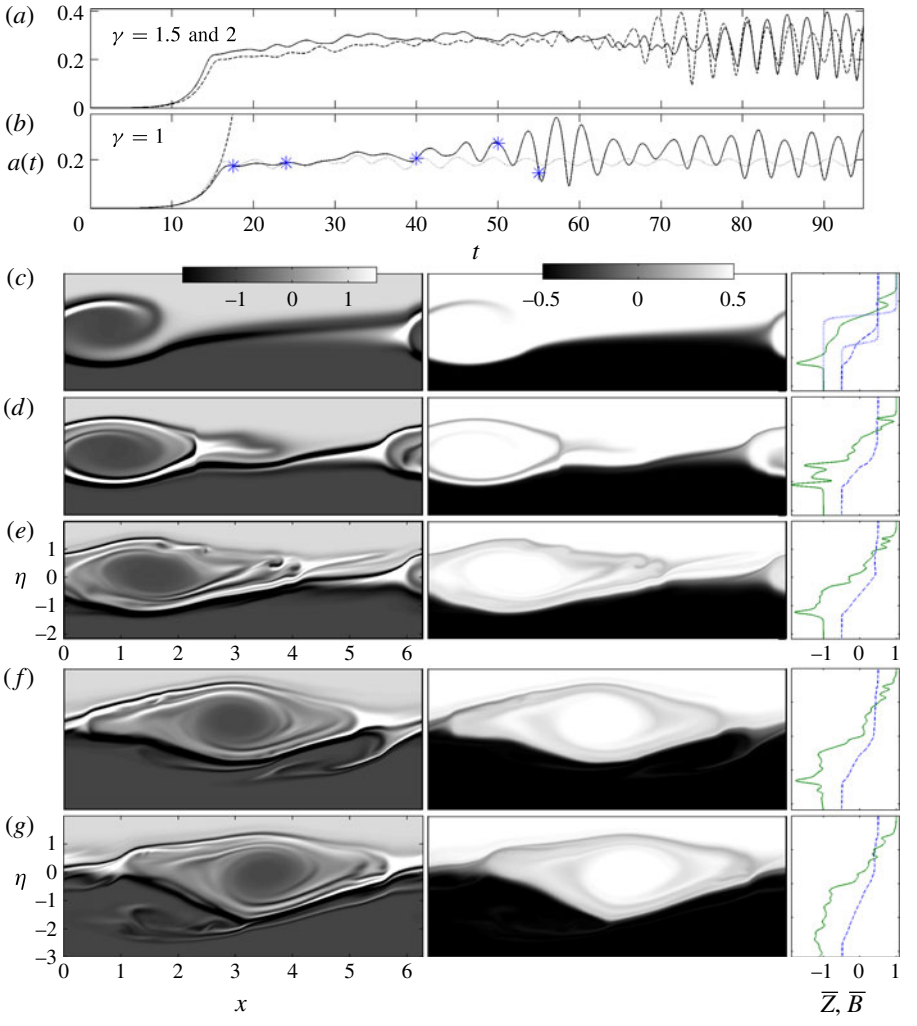


FIGURE 18. (Colour online) Numerical solution of one-sided Holmboe instability for (3.12) and (3.7), with $f = 2$, $\delta = 0.1$ and $\nu = 3\kappa = 10^{-3}$. The top panels show $a(t)$, for (*a*) $\gamma = 1.5$ and 2 and (*b*) $\gamma = 1$. In (*b*), the expected linear growth is shown as a dotted line, and the stars mark the instants at which the snapshots of $Z$ (left) and $B$ (right) are shown in (*c–g*), with horizontal averages of $Z$ (solid lines) and $B$ (dashed lines) displayed in the right-hand plots; the dotted lines in the first of these plots indicate the equilibrium profiles.

again suffer longer-wavelength secondary instabilities that trigger billow mergers. In both examples, the spatial pattern coarsens to a single billow.

Once more, the question arises as to whether coarsening continues as one further strengthens the stratification ($\gamma$). A partial answer to this question is provided by initial-value computations with $\gamma$ as high as 10 (and $\delta = 0.2$ and $\nu = \kappa = O(10^{-3})$). In these computations, coarsening continues uninterrupted to the fundamental mode, with varying initial forcings. For the non-propagating, symmetrical-in-$\eta$, Taylor states (and also the nonlinear KH modes) we may bolster such results with an explicit linear stability analysis (although different, this is based on an analysis of the Vlasov problem by Lin 2001). The details of the analysis are provided in appendix C. In

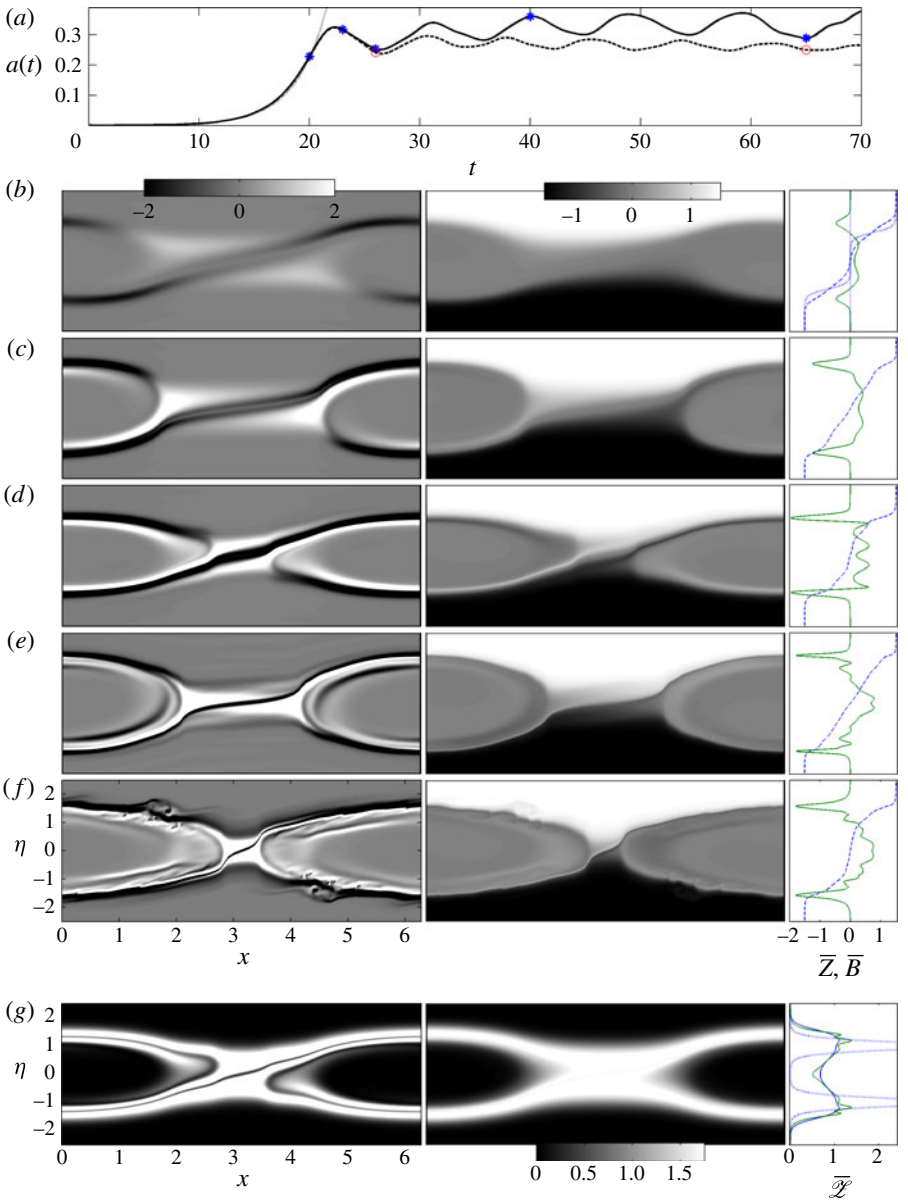


FIGURE 19. (Colour online) Numerical solution of the Taylor instability for (3.14) and (3.7), with $\gamma = 1.5$, $\delta = 0.2$ and $\nu = 3\kappa = 10^{-3}$. (*a*) shows $a(t)$, along with the expected linear growth (dotted line), and a second computation with $\nu = \kappa = 3.33 \times 10^{-4}$ (dashed line). The stars mark the instants at which the snapshots of $Z$ (left) and $B$ (right) are shown in (*b–f*); the circles mark the times of the two snapshots of $\mathscr{Z}$ shown in (*g*) for $\nu = \kappa = 3.33 \times 10^{-4}$. The right-hand plots show the horizontal averages of $Z$ (solid lines) and $B$ (dashed lines) in (*b–f*) and of $\mathscr{Z}$ (solid lines) for the two snapshots in (*g*); the dotted lines indicate the equilibrium profiles.

brief, we ignore diffusion and assume that the system has converged to a steady nonlinear wave with a given $(\Psi, \mathscr{Z})$-relation (cf. figure 20). It then becomes possible to show that this nonlinear wave equilibrium possesses an unstable linear normal

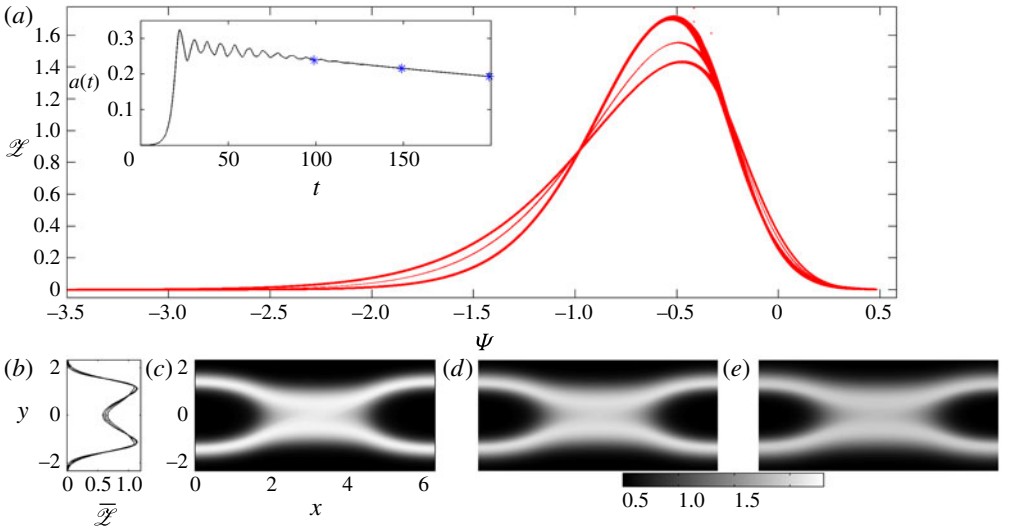


FIGURE 20. (Colour online) Taylor billows for $\gamma = 1.5$, $\delta = 0.2$ and $\nu = \kappa = 3.33 \times 10^{-4}$. (*a*) shows the slowly diffusing $(\Psi, \mathscr{Z})$-relation for the solutions at $t = 100$, 150 and 200. The corresponding horizontal averages and snapshots of $\mathscr{Z}$ are shown in (*b*,*c*). The time series of $a(t)$ is shown in the inset of (*a*).

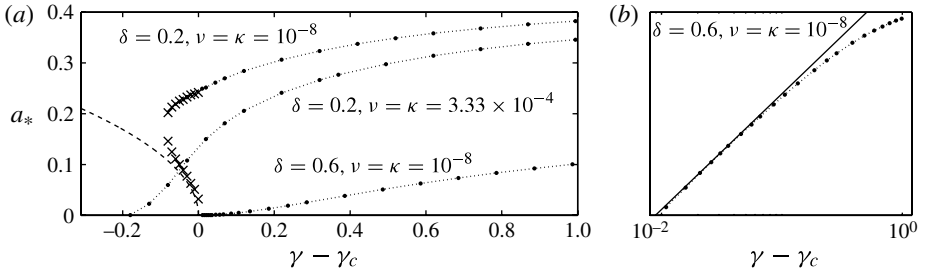


FIGURE 21. Saturation measure, $a_*$, against $\gamma$ for Taylor billows with $\delta = 0.2$ and $\delta = 0.6$ for $\nu = \kappa = 10^{-8}$, and $\delta = 0.2$ for $\nu = \kappa = 3.33 \times 10^{-4}$. In (*a*), the dashed line shows the unstable weakly nonlinear branch given by (B 16), and the crosses display $A_*^{(s)}$ and $A_*^{(u)}$ for subcritical states, computed as in figure 10 and § 4.1. The solid line in (*b*) shows the prediction of the single-wave model in (B 17).

mode if a certain integral is negative. The construction demonstrates the instability of the nonlinear states emerging from the initial-value problems with $\gamma < 10$ and two wavelengths in the domain. Unfortunately (and unlike the corresponding theory for the Vlasov problem), the need to compute the integral precludes us from confirming that waves with multiple wavelengths are always unstable, and there remains the possibility that coarsening becomes interrupted for larger $\gamma$. In any event, as noted in § 3.3, the defect theory does not capture the large-stratification cut-off to the Taylor instability.

The nonlinear waves described above are what one might call 'pure modes' as they are generated by linear modes with a unique wavenumber, $k$. However, a wide range of different varieties of nonlinear structures can be generated by using initial forcings that mix the Fourier modes. For example, figure 23 illustrates a long-lived state containing billows of unequal size generated by a mix of $k = 1$ and $k = 2$ forcing

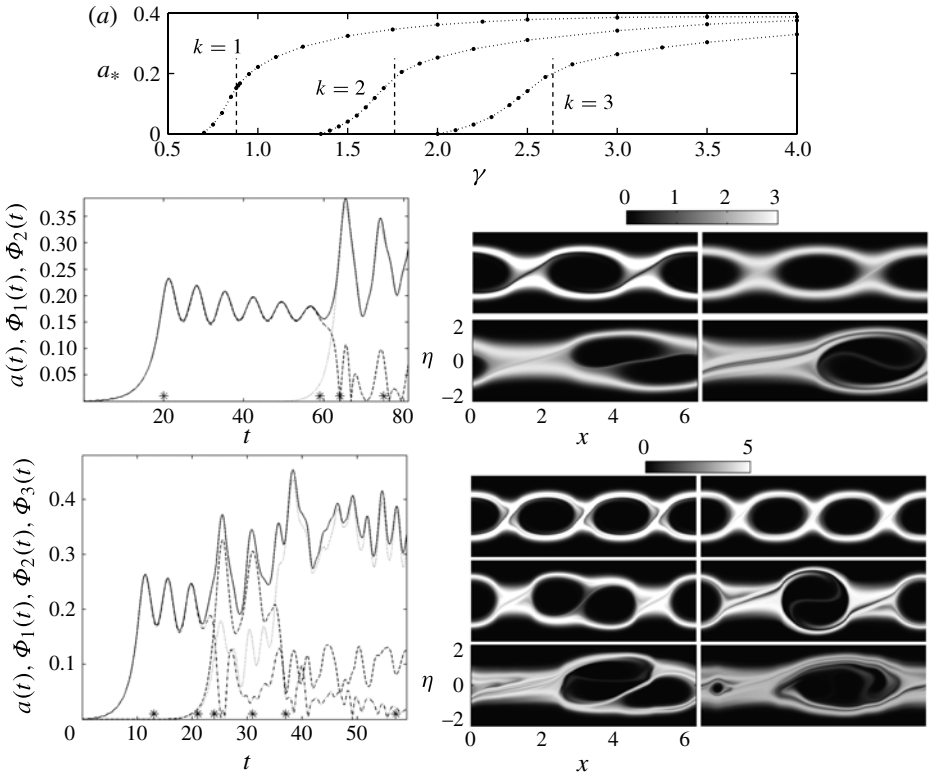


FIGURE 22. The top panel shows the 'bifurcation diagram' of the first three modes of Taylor instability for $\nu = \kappa = 3.33 \times 10^{-4}$ and $\delta = 0.2$, computed by adopting periodic domains of length, $2\pi/k$. The vertical dashed lines indicate the linear stability thresholds for $\nu = \kappa = 0$. Below are two computations showing merging of Taylor billows with $k = 2$ and 3 in periodic domains of length $2\pi$. In the first, with $\gamma = 1.9$, the streamfunction is forced by $(10^{-2}\delta_{n2} + 10^{-6}\delta_{n1})t\mathrm{e}^{-10t^2}$. For the second, with $\gamma = 3$, the forcing is $10^{-2}\delta_{n2}t\mathrm{e}^{-10t^2}$, and round-off error excite the fundamental mode. Shown on the left are time series of $a$ (solid lines), $\Phi_1$ (dotted lines), $\Phi_2$ (dashed lines) and $\Phi_3$ (dash-dotted lines; second computation only). The stars mark the times at which the snapshots of $\mathscr{Z}(x, \eta, t)$ are shown on the right.

terms. By selecting different relative strengths of the two forcing terms, it seems possible to generate mixed modes with an arbitrary degree of asymmetry between the billows. The transient state formed after the first merger of the $k = 3$ simulation in figure 22 shows another asymmetric mode, and Lee & Caulfield (2001) simulations with the Boussinesq equations display similar features. As for the higher-wavelength pure modes, the mixed modes do not survive indefinitely, but again suffer coarsening instabilities. Of course, this coarsening dynamics is purely two-dimensional, and may not carry over to three dimensions (a limitation that applies equally to the one-sided Holmboe dynamics summarized earlier).

A more curious kind of secondary instability is shown in figure 24, which illustrates the later-time dynamics of the computation shown earlier in figure 19. In this case, at the higher Prandtl number of $\nu/\kappa = 3$, the Taylor billows do not persist indefinitely like their (single-wavelength) counterparts with $\nu = \kappa$ shown in figure 20, which retain their structure whilst becoming smoothed by slow diffusion. Instead, after several pulsations the billows abruptly merge together to recreate a central mixed

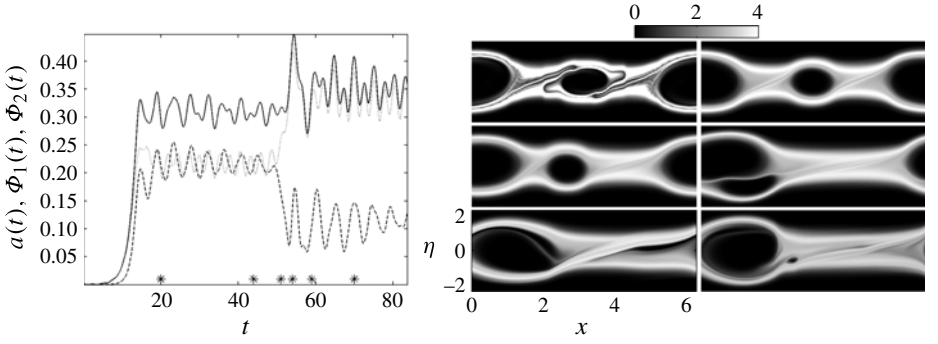


FIGURE 23. Merging of asymmetrical Taylor billows for $\nu = \kappa = 3.33 \times 10^{-4}$, $\gamma = 3$ and $\delta = 0.2$. The streamfunction of the initial state is forced by an additional term, $(10^{-2}\delta_{n1} + 10^{-4}\delta_{n2})te^{-10t^2}$. The time series of $a$ (solid line), $\Phi_1$ (dotted line) and $\Phi_2$ (dashed line) are shown in the left-hand plot, and the stars mark the times at which the snapshots of $\mathscr{Z}(x, \eta, t)$ are shown on the right.

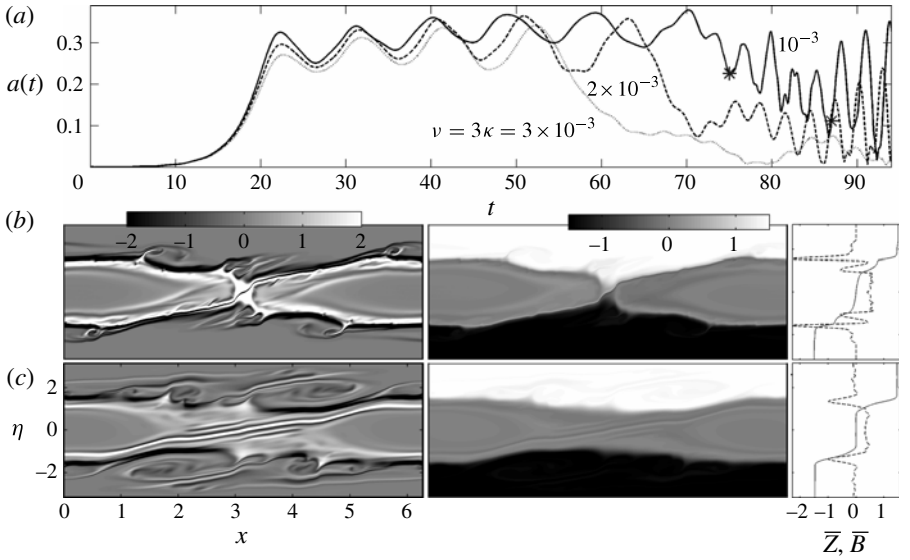


FIGURE 24. (Colour online) Continuation to longer times of the numerical solution shown in figure 19. (*a*) shows $a(t)$, along with corresponding solutions for $\nu = 3\kappa = 2 \times 10^{-3}$ (dashed lines) and $3 \times 10^{-3}$ (dotted lines). The stars indicate the times of the two snapshots shown in (*b*,*c*). The right-hand plots show the horizontal averages of $Z$ (solid lines) and $B$ (dashed lines).

layer of fluid. Unlike the initial state, however, that region is now bordered by strong filaments of vorticity and suffers secondary instabilities that resemble Holmboe waves. Simultaneously, the longer-period pulsations of the amplitude, $a(t)$, break down into irregular short-period oscillations. As illustrated by the computations with varying $\nu = 3\kappa$ also included in figure 24, the time of the breakdown is controlled by the level of diffusion.

## 5. Conclusion

The defect approximation furnishes a reduced model of the dynamics of two-dimensional stratified shear instabilities. In its simplest form, the model consists of a single evolution equation for a quantity (denoted by $\mathscr{Z}$ above) that combines the main effects of the defect's vorticity and buoyancy gradient, but is otherwise identical to the analogous formulation for unstratified defects. The model is also equivalent to a viscous version of the Vlasov–Poisson system of plasma physics (e.g. Nicholson 1983). The simplifications afforded by the model allow us to perform suites of well-resolved computations of flows with relatively sharp vorticity and density interfaces. We are thereby able to explore the nonlinear dynamics of three canonical types of stratified shear instability: the KH instability, the Holmboe instability and the Taylor instability. Within the defect framework, these instabilities are analogous to the Jeans instability of a self-gravitating sheet (Fujiwara 1981), and relatives of the bump-on-tail and two-stream instabilities (Nicholson 1983), respectively. Our stratified defects are also related to the 'grooves' and 'ridges' of accretion discs explored by Sellwood & Kahn (1991) (see also Lovelace *et al.* 2000).

We presented detailed results regarding the onset of the three types of instability. In particular, we outlined how the sharpness of the vorticity and density interfaces impacts onset. Relatively smooth interfaces lead to a gradual onset, with the saturation amplitude of instability following the 'trapping' scaling predicted by O'Neil *et al.* (1971) and fluid critical-layer theories (e.g. Churilov & Shukhman 1987). For sharper interfaces, however, the transition to instability is much more abrupt, and even becomes subcritical (with a nonlinear state existing below the linear instability threshold) as equilibrium interfaces approach the infinitely sharp (broken-line) limit. In this situation, the smoothing action of diffusion can be destabilizing. Our prediction of subcritical states has significant implications for the transient amplification recently found for linear Holmboe-wave dynamics (Constantinou & Ioannou 2011).

We also explored the dynamics of instabilities with more than one spatial wavelength. As is well-known, Kelvin–Helmholtz instabilities with multiple wavelengths suffer a vortex-pairing instability that leads to wave mergers. Here, we observed that Holmboe and Taylor instabilities can also suffer similar coarsening instabilities. A key detail of Holmboe wave dynamics is that these nonlinear structures are composed of vortices rolling up adjacent to a density interface; when that interface is sharp, the vortices largely sit inside unstratified fluid. Hence, the tendency of the Holmboe waves to merge is a reflection of familiar vortex dynamics. The Taylor 'billows' are rather different, consisting of mixed elliptical patches bordered by strong baroclinically generated vortex sheets. Nevertheless, a compact secondary stability theory can be provided for these nonlinear waves to demonstrate their tendency to coarsen (appendix C). We recorded two other types of secondary instabilities of the Holmboe waves and Taylor billows, neither of which have been previously observed. Both secondary instabilities appear for higher Prandtl number and take the form of additional Holmboe waves growing parasitically on the primary nonlinear structures. The significance of these secondary Holmboe instabilities to important practical processes such as mixing is unclear (especially given their two-dimensional character), although they are particularly destructive in the case of the Taylor billows. It is an interesting open question how such inherently two-dimensional secondary instabilities might interact with three-dimensional perturbations as a real flow evolves towards transition.

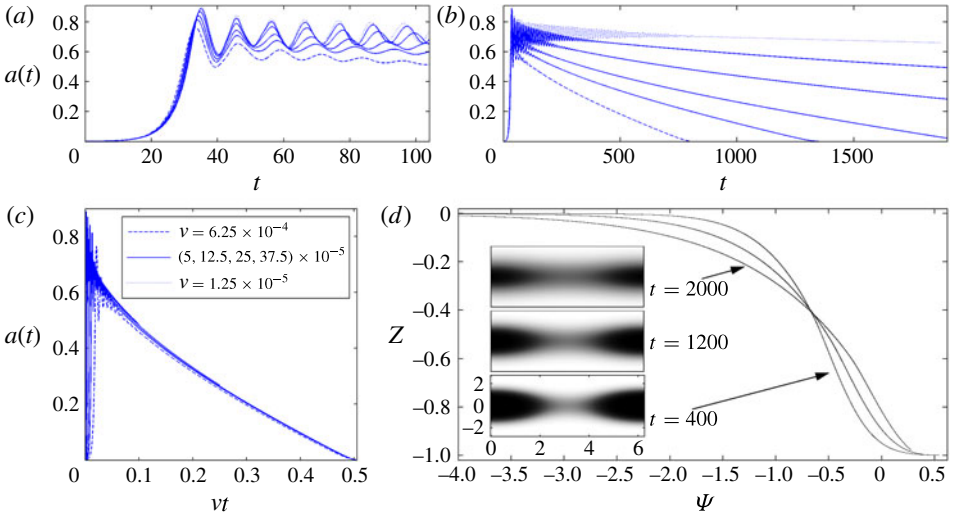


FIGURE 25. (Colour online) Numerical solutions of unstratified KH instability for $f = 2$, $\delta = 0.25$ and the values of $\nu$ indicated. (*a*,*b*) shows the short and long time trends of $a(t)$; (*c*) shows the same data against $\nu t$. (*d*), with $\nu = 1.25 \times 10^{-4}$, shows $Z$ against $\Psi$ for all points on the computational grid at the times indicated; insets show the corresponding snapshots of $Z(x, \eta, t)$.

## Acknowledgements

This work was partly performed at the 2010 Geophysical Fluid Dynamics Summer Study Program, which is held annually at Woods Hole Oceanographic Institution and supported by the National Science Foundation and Office of Naval Research. We thank the participants for discussions, especially P. Morrison.

## Appendix A. Long-time $\nu = \kappa$ dynamics

Mode amplitudes for long-time computations of unstratified KH instability with different values for $\nu$ are shown in figure 25. After the transient pulsations of the cat's eyes subside, the system evolves secularly in a manner that depends only on $\nu$ through the rescaled time, $T = \nu t$. Figure 25 plots $Z$ against $\Psi = \Phi - (1/2)\eta^2$ during this later viscous phase of evolution for the computation with $\nu = 1.25 \times 10^{-4}$; the vorticity–streamfunction relation is very tight, indicating strong relaxation to a quasisteady equilibrium with $Z = Z(\Psi)$.

To rationalize these numerical observations (and those in figure 20), we introduce the change of variables, $(x, \eta, t) \to (x, \Psi, T)$, which replaces the $\mathscr{Z}$-equation in (2.23) with

$$\mathscr{Z}_x = \nu \left[ (\eta \mathscr{Z}_\Psi)_\Psi - \eta^{-1} (\Phi_T \mathscr{Z}_\Psi + \mathscr{Z}_T) \right], \tag{A 1}$$

where $\eta(x, \Psi, T) = \sqrt{2[\Phi(x, T) - \Psi]}$. Since $\nu \ll 1$, the leading-order solution is independent of $x$. Introducing $\mathscr{Z} = F(\Psi) + \nu \mathscr{Z}_1(x, \Psi, T)$, and then integrating (A 1) in $x$ at fixed $\Psi$ to eliminate $\mathscr{Z}_1$ gives, to leading order in $\nu$,

$$[IF_\Psi]_\Psi = I_T F_\Psi - I_\Psi F_T, \tag{A 2}$$

where

$$I(\Psi, T) = \int_C \eta(x, \Psi, T)\,\mathrm{d}x \tag{A 3}$$

and $C$ denotes $(-\pi, \pi)$ for the open streamlines, or $(-X, X)$ with $\Phi(X, T) = \Psi$ (implying $\eta = 0$) for the closed streamlines within the cat's eyes. From (2.17), we also have

$$\mathscr{L}\Phi = 2\int_{-\infty}^{\Phi(x,T)} F(\Psi, T)\frac{\mathrm{d}\Psi}{\eta(x, \Psi, T)}. \tag{A 4}$$

Equations (A 2) and (A 4) furnish an integro-differential system for the slowly diffusing $\mathscr{Z}$–$\Psi$ relation.

## Appendix B. Weakly nonlinear analysis

### B.1. *Broken-line analysis*

In this appendix we perform a weakly nonlinear analysis of the inviscid defect model for a broken-line equilibrium profile, $\mathscr{Z} = H(\eta) \equiv F(\eta) - G_\eta(\eta)$. For brevity, we take $H(\eta)$ to be an even function and the unstable mode to be non-propagating (as in the KH and Taylor examples). We set the stage for the weakly nonlinear analysis by rescaling time, $T = \varepsilon t$, and introducing the decomposition, $\mathscr{Z} = H(\eta) + z(x, \eta, T)$, where $\langle z(x, \eta, T)\rangle = 0$. The inviscid defect model can then be written as

$$\eta z_x + \Phi_x H_\eta = -\varepsilon z_T - \Phi_x z_\eta, \quad \mathscr{L}\Phi = \int_{-\infty}^{\infty} z(x, \eta, t)\,\mathrm{d}\eta. \tag{B 1}$$

The horizontal average, $\overline{(\cdots)} = \int_0^{2\pi}(\cdots)\,\mathrm{d}x/2\pi$, of the first of these equations provides

$$\varepsilon\overline{z}_T = (\overline{\Phi z_x})_\eta\,. \tag{B 2}$$

Next, we pose the asymptotic sequences,

$$H = H_0 + \varepsilon^2 H_2, \quad z = \varepsilon z_1 + \varepsilon^2 z_2 + \cdots, \quad \Phi = \varepsilon\Phi_1 + \varepsilon^2\Phi_2 + \cdots, \tag{B 3}$$

Introducing these into (B 1) leads, at order $\varepsilon$, to the marginally unstable normal mode (with wavenumber $k = 1$),

$$z_1 = -\frac{H_{0\eta}\Phi_1}{\eta}, \quad \Phi = A(T)\mathrm{e}^{\mathrm{i}x} + c.c., \tag{B 4}$$

where $c.c.$ denotes complex conjugate, along with the marginal stability condition,

$$2 = \int_{-\infty}^{\infty} H_{0\eta}\frac{\mathrm{d}\eta}{\eta} \equiv I_1 \tag{B 5}$$

(satisfied by a judicious choice of parameters).

At order $\varepsilon^2$:

$$z_{2x} = -\frac{1}{\eta}(H_{0\eta}\Phi_{2x} + z_{1T} + \Phi_{1x}z_{1\eta}), \tag{B 6}$$

indicating

$$z_2 = \overline{z_2} - \frac{H_{0\eta}}{\eta}\Phi_2 - \frac{H_{0\eta}}{\eta^2}\Phi_{1xT} + \frac{1}{2}(\Phi_1^2 - \overline{\Phi_1^2})\frac{1}{\eta}\left(\frac{H_{0\eta}}{\eta}\right)_\eta. \tag{B 7}$$

Given the symmetry of the equilibrium profile,

$$\Phi_2 = -\frac{1}{4}(\Phi_1^2 - \overline{\Phi_1^2})I_3 = -\frac{1}{4}(A^2\mathrm{e}^{2\mathrm{i}x} + c.c.)I_3, \quad I_3 = \int_{-\infty}^{\infty} H_{0\eta}\frac{\mathrm{d}\eta}{\eta^3}, \tag{B 8}$$

and so

$$z_2 = \overline{z_2} - \frac{H_{0\eta}}{\eta^2}\Phi_{1xT} + \left[\frac{H_{0\eta}}{4\eta}I_3 + \frac{1}{2\eta}\left(\frac{H_{0\eta}}{\eta}\right)_\eta\right](A^2\mathrm{e}^{2\mathrm{i}x} + c.c.). \tag{B 9}$$

Also, in view of (B 4), the first non-trivial result from (B 2) is

$$\overline{z_2}_T = (\overline{\Phi_1 z_{2x} + \Phi_2 z_{1x}})_\eta = \left(\frac{H_{0\eta}}{\eta^2}\right)_\eta (|A|^2)_T, \tag{B 10}$$

implying

$$\overline{z_2} = \left(\frac{H_{0\eta}}{\eta^2}\right)_\eta (|A|^2 - |A_0|^2), \tag{B 11}$$

if $A(0) = A_0$ and $\overline{z_2}(\eta, 0) = 0$.

Finally, at $O(\varepsilon^3)$:

$$z_{3x} = -\frac{1}{\eta}(H_{0\eta}\Phi_{3x} + H_{2\eta}\Phi_{1x} + z_{2T} + \Phi_{2x}z_{1\eta} + \Phi_{1x}z_{2\eta}). \tag{B 12}$$

Isolating the contribution of the right-hand side to the first Fourier mode, $\mathrm{e}^{\mathrm{i}x}$, and then applying the second relation in (B 1) leads to the amplitude equation,

$$I_3 A_{TT} = JA + \tfrac{1}{4}(I_3^2 + 2I_5)|A|^2 A, \tag{B 13}$$

with

$$J = \int_{-\infty}^{\infty} H_{2\eta}\frac{\mathrm{d}\eta}{\eta} - 2I_5|A_0|^2, \quad I_5 = \int_{-\infty}^{\infty} H_{0\eta}\frac{\mathrm{d}\eta}{\eta^5}. \tag{B 14}$$

We now take $|A_0| \ll 1$. For the Kelvin–Helmholtz case, with $f = 1 + \varepsilon^2 f_2$, $\gamma = 0$ and $H_\eta = f[\delta(\eta - 1) - \delta(\eta + 1)]$, the integrals, $I_1 = I_3 = I_5 = 2$ and $J = 2f_2$, giving

$$A_{TT} = f_2 A + |A|^2 A. \tag{B 15}$$

For the Taylor case, with $f = 0$, $\gamma = 1 + \varepsilon^2\gamma_2$ and $H = \gamma[\delta(\eta - 1) + \delta(\eta + 1)]$, we have $I_1 = 2$, $J = 2\gamma_2$, $I_3 = 6$ and $I_5 = 10$, leading to

$$A_{TT} = \frac{\gamma_2}{3}A + \frac{7}{3}|A|^2 A. \tag{B 16}$$

In both cases, the nonlinear terms are destabilizing and the bifurcation is subcritical. Note that the integrals $I_3$ and $I_5$ do not exist if $H_0(\eta)$ is a smooth function with non-zero higher derivatives at $\eta = 0$.

### B.2. *Critical-layer theory*

When the critical-level singularities at $\eta = 0$ cannot be removed by suitably arranging the derivatives of $H(\eta)$ to vanish, a different asymptotic scheme is needed to that followed above. The details follow along the guidelines presented by Churilov & Shukhman (1987) and Shukhman & Churilov (1997); a derivation more aligned to our

defect model is given by Balmforth *et al.* (2012). We skip to the main conclusions: the problems posed by the critical-level singularities force one to abandon a conventional weakly nonlinear expansion in a narrow region around $\eta = 0$ (the critical layer) and search for a different solution there. That solution can be matched to the standard weakly nonlinear solution, which remains valid outside the critical layer. Unfortunately, there is no analytical solution for the critical layer, and one must still solve a nonlinear partial differential equation much like the original defect equation. Thus, the theory is less explicit and demands a numerical component. Also, the scalings in $\varepsilon$ that are required in the theory are different to those in (B 2). In particular, $z$ and $\Phi$ are order $\varepsilon^2$, whereas $H = H_0 + \varepsilon H_1$; this is the trapping scaling of O'Neil *et al.* (1971). After numerically solving the critical-layer problem, we find an estimate for the first maximum in $a(t)$:

$$a_* \sim \frac{0.52}{[H_{0\eta\eta}(0)]^2}\left[\int_{-\infty}^{\infty}[H(\eta) - H_0(\eta)]_\eta \,\frac{\mathrm{d}\eta}{\eta}\right]^2. \tag{B 17}$$

## Appendix C. Secondary instability

Consider a stationary nonlinear wave given by

$$\Phi = \Xi(x), \quad \mathscr{Z} = \mathscr{F}(\Psi), \quad \Psi = \Xi(x) - \tfrac{1}{2}\eta^2. \tag{C 1}$$

Normal-mode perturbations about this state with the form,

$$\Phi = \Xi(x) + \xi(x)\mathrm{e}^{\lambda t}, \quad \mathscr{Z} = \mathscr{F}(\Psi) + \sigma(x,\eta)\mathrm{e}^{\lambda t}, \tag{C 2}$$

satisfy

$$\lambda\sigma + \eta\sigma_x + \Xi_x\sigma_\eta = \eta\mathscr{F}_\Psi\xi_x, \quad \mathscr{L}\xi = \int_{-\infty}^{\infty}\sigma\,\mathrm{d}\eta. \tag{C 3}$$

As shown by Lin (2001), if $\lambda$ is real and positive, then the first of these equations can be solved for $\sigma$ in terms of $\xi$ using the method of characteristics. Formally, we write

$$\int_{-\infty}^{\infty}\sigma\,\mathrm{d}\eta = \mathscr{K}_\lambda\xi, \tag{C 4}$$

where $\mathscr{K}_\lambda$ is an operator that integrates $\xi(x)$ over the characteristics, and which are equivalent to the streamlines, $\Psi = \textit{constant}$, of the nonlinear wave. The specific wave solutions of interest possess two families of streamlines: the closed streamlines within the cat's eyes and the open streamlines above and below.

The equation determining $\xi$ now becomes $(\mathscr{K}_\lambda - \mathscr{L})\xi = 0$. Lin (2001) establishes that $\mathscr{K}_\lambda$ (for $\lambda$ real and positive) is self-adjoint. Next consider the associated eigenvalue problem,

$$(\mathscr{K}_\lambda - \mathscr{L})w = \Lambda w, \tag{C 5}$$

for which

$$\Lambda(\lambda) = \mathscr{R}[w] = \frac{\displaystyle\int_0^{2\pi} w(\mathscr{K}_\lambda - \mathscr{L})w\,\mathrm{d}x}{\displaystyle\int_0^{2\pi} w^2\,\mathrm{d}x}. \tag{C 6}$$

Note that, from (C 3), $\sigma \sim O(\lambda^{-1})$ for $\lambda \gg 1$, and so the eigenvalues of $\mathscr{K}_\lambda - \mathscr{L} \sim -\mathscr{L}$ are $\Lambda \sim 2k$ in this limit. Moreover, because each $\Lambda(\lambda)$ is a continuous function, if we can establish that the smallest associated eigenvalue, $\Lambda_0(\lambda)$, is negative for $\lambda \to 0$ (from above), then there must be an intermediate value of $\lambda$ for which that eigenvalue vanishes. That is, there must be an unstable mode.

In the Vlasov version of the problem considered by Lin (2001), the analogue of (C 6) contains the differential operator, $\partial_x^2$, rather than our integral operator $\mathscr{L}$. This precludes us from exploiting the Sturmian theory of ordinary differential equations (ODEs), which is the last piece of the proof of instability provided by Lin. Instead, to show that $\Lambda_0(0) < 0$, we use the variational form of the associated eigenvalue problem. In particular, if the right-hand side of (C 6) can be evaluated and shown to be negative using a suitable trial function, then the result is established since the actual associated eigenvalue must be smaller.

Thus, we require the limiting form of $\mathscr{K}_\lambda w$ for $\lambda \to 0$. This form can be found by introducing the expansion $\sigma = \sigma_0 + \lambda\sigma_1 + \cdots$ into (C 3). We find

$$\eta\sigma_{0x} + \Xi_x\sigma_{0\eta} = \eta\mathscr{F}_\Psi w_x, \quad \eta\sigma_{1x} + \Xi_x\sigma_{1\eta} = -\sigma_0. \tag{C 7}$$

By transforming from $(x, \eta)$ to a new set of coordinates based on the streamlines, $(x, \Psi)$, these equations may be rewritten as

$$\sigma_{0x} = \mathscr{F}_\Psi w_x, \quad \sigma_{1x} = -\frac{1}{\eta}\sigma_0, \tag{C 8}$$

where $\eta(x, \Psi) = \pm\sqrt{2(\Xi - \Psi)}$. Thus, $\sigma_0 = \Sigma(\Psi) + w\mathscr{F}_\Psi$, where the arbitrary function of integration, $\Sigma(\Psi)$, can be determined by observing that the integral of $\sigma_{1x}$ along the complete circuit of any of the characteristic curves must vanish. That is, $\oint \sigma_0\,\mathrm{d}x/\eta = 0$, if we denote by $\oint(\cdots)\,\mathrm{d}x$ the integral across the periodic domain $(0 \leqslant x \leqslant 2\pi)$ or around the closed streamlines for the two families of characteristics. To be more definitive, suppose that there are $N$ wavelengths of the steady nonlinear solution within the domain. Then there are $N$ intervals in $x$ corresponding to each cat's eye for a given $\Xi_{max} \geqslant \Psi \geqslant \Xi_{min}$, which we denote as $I_k$, $k = 1, \ldots, N$ (see figures 26 and 27). For each value of $\Psi$ within this range, $\Sigma = -\mathscr{F}_\Psi W_k$ and $\sigma_0 = (\xi - W_k)\mathscr{F}_\Psi$, if $x \in I_k$, where

$$\left.\begin{aligned} W_k &= \frac{2}{\Pi}\int_{I_k} \frac{w(x)\,\mathrm{d}x}{\sqrt{2[\Xi(x) - \Psi]}}, \\ \Pi &= 2\int_{I_k} \frac{\mathrm{d}x}{\sqrt{2[\Xi(x) - \Psi]}} = 2\int_{x_1}^{x_2} \frac{\mathrm{d}x}{\sqrt{2[\Xi(x) - \Psi]}}, \end{aligned}\right\} \tag{C 9}$$

and $I_1 = [x_1, x_2]$, as in figures 26 and 27. Above or below the cat's eyes ($\Psi < \Xi_{min}$), on the other hand, $\Sigma = (\xi - W)\mathscr{F}_\Psi$ with

$$W = \frac{1}{\Pi}\int_0^{2\pi} \frac{w(x)\,\mathrm{d}x}{\sqrt{2[\Xi(x) - \Psi]}}, \quad \Pi = \int_0^{2\pi} \frac{\mathrm{d}x}{\sqrt{2[\Xi(x) - \Psi]}}. \tag{C 10}$$

We now change variables, $(x, \eta) \to (x, \Psi)$, in the double integral, $\int_0^{2\pi}\int_{-\infty}^{\infty}(\cdots)\,\mathrm{d}\eta\,\mathrm{d}x$, contained in the numerator of $\mathscr{R}[w]$, to write

$$\mathscr{R}[w] = \frac{\displaystyle\int_0^{2\pi} w(V - \mathscr{L})w\,\mathrm{d}x + \mathscr{R}_C}{\displaystyle\int_0^{2\pi} w^2\,\mathrm{d}x} \tag{C 11}$$

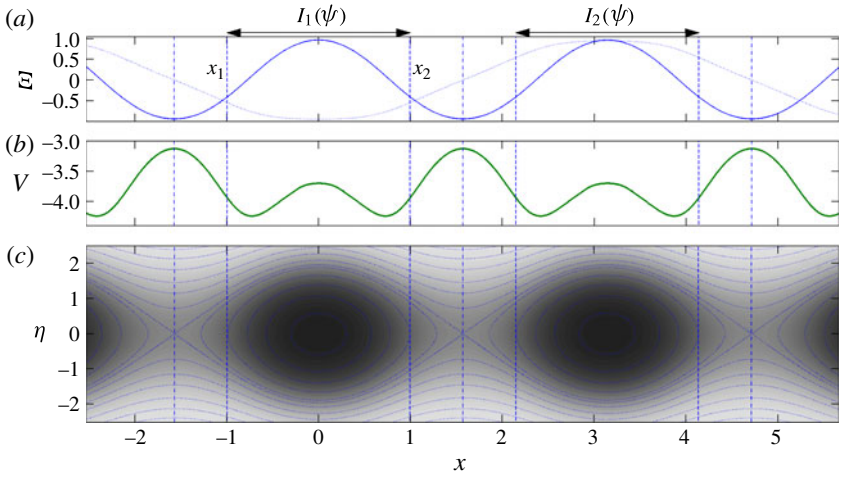


FIGURE 26. (Colour online) Slowly diffusing, long-time, KH solution with $f = 4$, $\delta = 1$, $\gamma = 0$, $\nu = 10^{-3}$ and $\varepsilon_0 = 10^{-4}$, in a domain of length $\pi$. Two wavelengths of the final ($t = 100$) solution are shown; ($a$) displays $\Xi(x)$, ($b$) plots the potential $V(x)$ computed using (C 15), and ($c$) shows contours of constant $\Psi$ with shading corresponding to $Z(x, \eta, t)$. In ($a$), the dotted curve shows the eigenfunction corresponding to the smallest eigenvalue of $(\mathscr{L}^{-1}V - 1)w = \Lambda\mathscr{L}^{-1}w$. The vertical dashed lines in each panel show the borders of the intervals $I_k$, $k = 1$ and 2 ($I_1 = [x_1, x_2]$), for a particular value of $\Psi$ corresponding to one of the closed contour levels in ($c$).

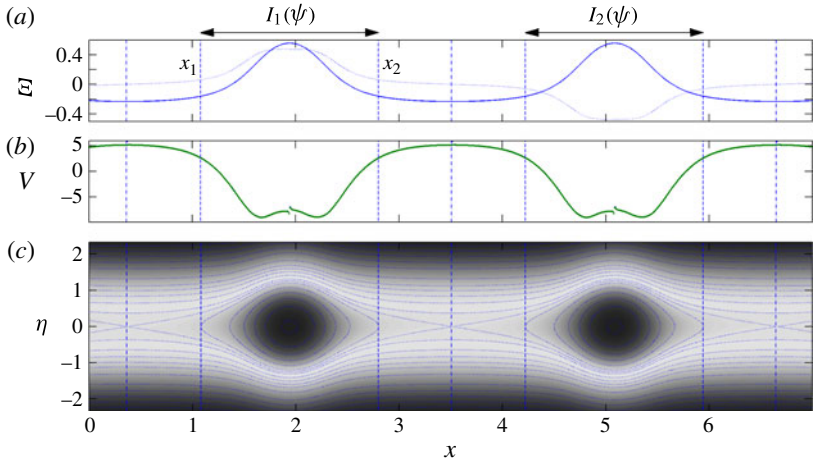


FIGURE 27. (Colour online) A similar picture to figure 26, but for a solution at $t = 90$ generated by the Taylor instability with $\gamma = 8$, $\delta = 0.2$, $\nu = \kappa = 2 \times 10^{-3}$ and $\varepsilon = 10^{-4}$, in a domain of length $\pi$.

where

$$V(x) = \int_{-\infty}^{\infty} \mathscr{F}_{\Psi}(\Psi)\, \mathrm{d}\eta \tag{C 12}$$

and

$$\mathscr{R}_C = -\int_{-\infty}^{\Xi_{min}} \mathscr{F}_\Psi W^2 \,\mathrm{d}\Psi - \int_{\Xi_{min}}^{\Xi_{max}} \mathscr{F}_\Psi \sum_{k=1}^{N} W_k^2 \,\mathrm{d}\Psi. \tag{C 13}$$

Note that the nonlinear wave itself satisfies

$$\mathscr{L}\Xi = \int_{-\infty}^{\infty} \mathscr{F}(\Psi)\,\mathrm{d}\eta, \tag{C 14}$$

implying

$$V \equiv \frac{1}{\Xi_x}\frac{\partial}{\partial x}\int_{-\infty}^{\infty} \mathscr{F}(\Psi)\,\mathrm{d}\eta \equiv \frac{\mathscr{L}\Xi_x}{\Xi_x}. \tag{C 15}$$

For the KH solutions, $\mathscr{F}_\Psi < 0$ (see figure 8). Thus, $\mathscr{R}_C$ impedes us establishing that $\Lambda(0) < 0$. This contribution also significantly complicates efforts to work with $\mathscr{R}[w]$. To make progress, we therefore consider nonlinear waves with two wavelengths in the domain, as in figures 26–27, and adopt trial functions for $w(x)$ which have the opposite symmetry to $\Xi$ with regard to the centres of the cat's eyes. This choice guarantees that $\mathscr{R}_c = 0$ in view of the form of the integrals $W_k$ and $W$, and is straightforward to arrange: with a suitable shift of $x$, both the KH and Taylor solutions in figures 26–27 can be written as Fourier series, $\sum_{n=1}^{\infty} \Xi_n \cos 2nx$; it then suffices to take $w = \sum_{n=1}^{\infty} w_n \cos(2n-1)x$. Thus, we are left with

$$\mathscr{R}[w] \to \frac{\displaystyle\int_0^{2\pi} w(V-\mathscr{L})w\,\mathrm{d}x}{\displaystyle\int_0^{2\pi} w^2\,\mathrm{d}x}. \tag{C 16}$$

A simple trial function is $\cos(x - x_s)$, where $x_s$ denotes the centre of one of the cat's eyes. For the two solutions presented in figures 26–27, and given the potential function $V(x)$ computed via (C 15), we then find that $\Lambda(0) < -1.93$ or $-2.3$, respectively. Note that we may further compute the actual smallest eigenvalues of the eigenvalue problem, $(\mathscr{L}^{-1}V - 1)w = \Lambda(0)\mathscr{L}^{-1}w$ using a simple discretization of $x$ and quadrature rule for the integral in $\mathscr{L}^{-1}$ (exploiting the Fourier series representation of this operator). This calculation implies that $\Lambda(0) \approx -1.94$ and $-4.6$; the corresponding eigenvectors (which have the correct symmetry to ensure that $\mathscr{R}_C = 0$) are also plotted in figures 26–27. For the KH example, the eigenvector's shape is close to $\cos x$, and the variational estimate of $\Lambda(0)$ is close to the computed eigenvalue. The estimate for $\Lambda(0)$ is rather worse for the Taylor case because of the relatively non-sinusoidal form of its potential $V(x)$. In any event, via a straightforward computation, we establish the instability of the two solutions towards normal modes with twice the wavelength; i.e. coarsening modes.

Low-amplitude waves provide another illustration of the construction of $\mathscr{R}[w]$. For these solutions, $\Xi \sim a\cos Nx$, and if $N$ is even, we may take $w = \cos(Nx/2)$ to guarantee that $\mathscr{R}_C = 0$. Moreover, $V \sim -2N$, and so $\mathscr{R} \to -N < 0$. i.e. sufficiently low-amplitude waves are always unstable to modes with twice the wavelength.

## REFERENCES


ALEXAKIS, A. 2005 On Holmboe's instability for smooth shear and density profiles. *Phys. Fluids* **17**, 084103.

BAINES, P. G. & MITSUDERA, H. 1994 On the mechanism of shear flow instabilities. *J. Fluid Mech.* **276**, 327–342.

BALMFORTH, N. J. 1998 Stability of vorticity defects in viscous shear. *J. Fluid Mech.* **357**, 199–224.

BALMFORTH, N. J., DEL CASTILLO-NEGRETE, D. & YOUNG, W. R. 1997 Dynamics of vorticity defects in shear. *J. Fluid Mech.* **333**, 197–230.

BALMFORTH, N. J., MORRISON, P. J. & THIFFEAULT, J.-L. 2012 Pattern formation in systems with continuous spectra and the single-wave model. *Rev. Mod. Phys.* (to be submitted).

BROWN, S. N. & STEWARTSON, K. 1978 The evolution of the critical layer of a Rossby wave. Part II. *Geophys. Astrophys. Fluid Dyn.* **10**, 1–24.

CARPENTER, J. R., BALMFORTH, N. J. & LAWRENCE, G. A. 2010*a* Identifying unstable modes in stratified shear layers. *Phys. Fluids* **22**, 054104.

CARPENTER, J. R., TEDFORD, E. W., RAHMANI, M. & LAWRENCE, G. A. 2010*b* Holmboe wave fields in simulation and experiment. *J. Fluid Mech.* **648**, 205–223.

CAULFIELD, C. P. 1994 Multiple linear instability of layered stratified shear flow. *J. Fluid Mech.* **258**, 255–285.

CAULFIELD, C. P. & PELTIER, W. R. 2000 The anatomy of the mixing transition in homogeneous and stratified free shear layers. *J. Fluid Mech.* **413**, 1–47.

CAULFIELD, C. P., YOSHIDA, S., PELTIER, W. R. & OHTANI, M. 1995 An experimental investigation of the instability of a shear flow with multi-layer density stratification. *Phys. Fluids* **7**, 3028–3041.

CHENG, C. Z. & KNORR, G. 1976 Integration of Vlasov equation in configuration space. *J. Comput. Phys.* **22**, 330–351.

CHURILOV, S. M. & SHUKHMAN, I. G. 1987 Nonlinear stability of a stratified shear-flow – a viscous critical layer. *J. Fluid Mech.* **180**, 1–20.

CHURILOV, S. M. & SHUKHMAN, I. G. 1996 The nonlinear critical layer resulting from the spatial or temporal evolution of weakly unstable disturbances in shear flows. *J. Fluid Mech.* **318**, 189–221.

CONSTANTINOU, N. C. & IOANNOU, P. J. 2011 Optimal excitation of two-dimensional Holmboe instabilities. *Phys. Fluids* **23**, 074102.

CORCOS, G. M. & SHERMAN, F. S. 1976 Vorticity concentration and the dynamics of unstable free shear layers. *J. Fluid Mech.* **73**, 241–264.

FUJIWARA, T. 1981 Vlasov simulations of stellar systems: infinite homogeneous case. *Publ. Astron. Soc. Japan* **33**, 531–540.

GILL, A. E. 1965 A mechanism for instability of plane Couette flow and of Poiseuille flow in a pipe. *J. Fluid Mech.* **21**, 503–511.

HOGG, A. M. & IVEY, G. N. 2003 The Kelvin–Helmholtz to Holmboe instability transition in stratified exchange flows. *J. Fluid Mech.* **477**, 339–362.

HOLMBOE, J. 1962 On the behaviour of symmetric waves in stratified shear layers. *Geophys. Publ.* **24**, 67–113.

IVEY, G. N., WINTERS, K. B. & KOSEFF, J. R. 2008 Density stratification, turbulence, but how much mixing? *Annu. Rev. Fluid Mech.* **40**, 169–184.

KLAASSEN, G. P. & PELTIER, W. R. 1989 The role of transverse secondary instabilities in the evolution of free shear layers. *J. Fluid Mech.* **202**, 367–402.

LEE, V. & CAULFIELD, C. P. 2001 Nonlinear evolution of a layered stratified shear flow. *Dyn. Atmos. Oceans* **34**, 103–124.

LIN, Z. 2001 Instability of periodic BGK waves. *Math. Res. Lett.* **8**, 1–14.

LINDEN, P. F. 1979 Mixing in stratified fluids. *Geophys. Astrophys. Fluid Dyn.* **13**, 2–23.

LOVELACE, R. V. E., LI, H., COLGATE, S. A. & NELSON, A. F. 2000 Rossby wave instability of Keplerian accretion disks. II. Detailed linear theory. *Astrophys. J.* **533**, 1023–1034.

MASHAYEK, A. & PELTIER, W. R. 2011*a* Turbulence transition in stratified atmospheric and oceanic shear flows: Reynolds and Prandtl number controls upon the mechanism. *Geophys. Res. Lett.* **38**, L16612.

MASHAYEK, A. & PELTIER, W. R. 2011*b* Three-dimensionalization of the stratified mixing layer at high Reynolds number. *Phys. Fluids* **23**, 111701.

NICHOLSON, D. R. 1983 *Introduction to Plasma Theory*. Wiley.

O'NEIL, T. M., WINFREY, J. H. & MALMBERG, J. H. 1971 Nonlinear interaction of a small cold beam and a plasma. *Phys. Fluids* **14**, 1204–1212.

PELTIER, W. R. & CAULFIELD, C. P. 2003 Mixing efficiency in stratified shear flows. *Annu. Rev. Fluid Mech.* **35**, 135–167.

RAHMANI, M. 2011 Kelvin–Helmholtz instability in sheared density stratified flows, PhD thesis, University of British Columbia.

SCHMITT, R. W. 1994 Double diffusion in oceanography. *Annu. Rev. Fluid Mech.* **26**, 255–285.

SELLWOOD, J. A. & KAHN, F. D. 1991 Spiral modes driven by narrow features in angular-momentum density. *Mon. Not. R. Astron. Soc.* **250**, 278–299.

SHUKHMAN, I. G. & CHURILOV, S. M. 1997 Effect of slight stratification on the nonlinear spatial evolution of a weakly unstable wave in a free shear layer. *J. Fluid Mech.* **343**, 197–233.

SMYTH, W. D., KLAASSEN, G. P. & PELTIER, W. R. 1988 Finite amplitude Holmboe waves. *Geophys. Astrophys. Fluid Dyn.* **43**, 181–222.

SMYTH, W. D. & MOUM, J. N. 2000 Length scales of turbulence in stably stratified mixing layers. *Phys. Fluids* **12**, 1327–1342.

SMYTH, W. D. & WINTERS, K. B. 2003 Turbulence and mixing in Holmboe waves. *J. Phys. Oceanogr.* **33**, 649–671.

STAQUET, C. 1995 Two-dimensional secondary instabilities in a strongly stratified shear layer. *J. Fluid Mech.* **296**, 73–126.

STAQUET, C. 2000 Mixing in a stably stratified shear layer: two- and three-dimensional numerical experiments. *Fluid Dyn. Res.* **27**, 367–404.

SUTHERLAND, B. R. 2010 *Internal Gravity Waves*. Cambridge University Press.

TAYLOR, G. I. 1931 Effect of variation in density on the stability of superposed streams of fluid. *Proc. R. Soc. Lond.* A **132**, 499–523.

TEDFORD, E. W., PIETERS, R. & LAWRENCE, G. A. 2009 Symmetric Holmboe instabilities in a laboratory exchange flow. *J. Fluid Mech.* **636**, 137–153.

THORPE, S. A. 1971 Experiments on instability of stratified shear flows: miscible fluids. *J. Fluid Mech.* **46**, 299–319.

WINANT, C. D. & BROWAND, F. K. 1974 Vortex pairing: the mechanism of turbulent mixing-layer growth at moderate Reynolds number. *J. Fluid Mech.* **63**, 237–255.

YOSHIDA, S., OHTANI, M., NISHIDA, S. & LINDEN, P. F. 1998 Mixing processes in a highly stratified river. In *Physical Processes in Lakes & Oceans* (ed. J. Imberger). *Coastal & Estuarine Studies*, vol. 54. pp. 389–400. American Geophysical Union.

ZHU, D. & LAWRENCE, G. A. 2001 Holmboe's instability in exchange flows. *J. Fluid Mech.* **429**, 391–401.